

# An isogeometric implicit $G^1$ mixed finite element for Kirchhoff space rods

L. Greco<sup>b,c</sup>, M. Cuomo<sup>a,c,\*</sup>

<sup>a</sup> *Department of Civil Engineering and Architecture, University of Catania, viale A. Doria 6, 95100 Catania, Italy*

<sup>b</sup> *Department of Civil, Building-Architecture, Environmental Engineering, DICEAA, University of L'Aquila, Italy*

<sup>c</sup> *International Research Center on Mathematics and Mechanics of Complex System, M&MOCS, Cisterna di Latina, Italy*

---

## Highlights

- The performance of an isogeometric multipatch formulation for Kirchhoff space rods with respect to membrane and flexural locking is analysed.
- A mixed formulation is proposed in the spirit of the B-bar method.
- It is shown that the mixed formulation is able to almost avoid locking.
- The optimal rate of convergence is recovered for interpolation degrees higher than 2.
- The mixed formulation yields accurate results for the internal forces, differently from the pure displacement formulation.

---

## Abstract

In the paper we present a multi patch isogeometric mixed element with implicit geometric continuity at the ends for the analysis of non polar Kirchhoff space rods. Rotations are introduced at the ends of the element analogously to the *Hermitian* interpolation, performing a change of basis for the configuration space. A mixed method in which the internal forces are interpolated by means of an  $L^2$  projection leading to a  $\bar{B}$  formulation is used to cope with the membrane–flexural locking that affects the solution. The efficiency of the method in avoiding locking and instabilities is investigated. The formulation adopted has the advantage with respect to other formulations that a non full global stiffness matrix is obtained. This approach appears very appealing for efficient analyses of general assemblies of 3D non polar elements.

*Keywords:* Kirchhoff space rod; Isogeometric analysis; Geometric continuity; B-bar method; Membrane locking; Flexural locking

---

## 1. Introduction

Kirchhoff rods are spatial non polar rods, whose initial geometry can be affected by flexural and/or torsional curvatures, and whose internal energy is due to axial, bending and torsional deformations. A 4-dimensional

---

\* Corresponding author at: Department of Civil Engineering and Architecture, University of Catania, viale A. Doria 6, 95100 Catania, Italy. Tel.: +39 0957382263.

*E-mail addresses:* [leopoldo.greco@virgilio.it](mailto:leopoldo.greco@virgilio.it) (L. Greco), [mcuomo@dica.unict.it](mailto:mcuomo@dica.unict.it) (M. Cuomo).

configuration space is necessary for modelling the Kirchhoff rod (the centroid curve position vector and the torsional angle) [1,2]. In the literature this kind of manifold is also known as ribbon, see [3].

Kirchhoff rod models have the advantage, with respect to shear deformable models, that shear locking is automatically avoided. Furthermore, it is used for modelling particular spatial structures, like cables with bending and torsional stiffness; for instance, in [4] the authors present a bending-stabilized cable model, while in [5,6] the authors consider the effect of torsional stiffness in aeroelastic analysis.

In [1] a geometrically exact formulation of space rods based on a Lagrangian description was presented, that does not depend on the particular geometry of the centroid curve (differently from what has been done for instance in [7–10]). An orthogonal frame was introduced on the rod axis, that can be different from the natural frame (Bishop frame) used by Langer and Singer [11]. A pull-back of the strain along the directors was used to define the deformation of the cross section, analogously to what is done in non local and second gradient theory, i.e. [12–17].

Since high continuity is required for the interpolation of the displacements in a Kirchhoff–Love rod model, the B-spline interpolation used in isogeometric analysis appears to be a natural choice for the development of numerical approximations of thin structural models. A first example of isogeometric interpolation for non polar rods can be found in [18] in which the authors have considered the polar formulation of rods developed in [19]. Many others numerical isogeometric formulations for rods have been proposed since (see, e.g., [20–25]).

When multiple elements are used for discretizing the model,  $C^0$  continuity for the end rotations of the element is needed, that for the Kirchhoff rod model means a  $G^1$  continuity constraint on the deformation of the centroid curve, i.e., the unit tangent vectors have to coincide at the ends of adjacent elements; from an incremental point of view this means that the velocity of rotation at the ends of adjacent elements must be equal.

In [26,27]  $G^1$  continuity for space rods was obtained by means of a change of basis, generalizing Hermite’s interpolation. The required geometric continuity was thus achieved without introducing Lagrangian or penalty terms in the formulation, as done for instance by the bending strip method [28]. An alternative strategy of a multi-patch approach for non polar shells can be found in [29].

Although it has been claimed that sufficiently high degrees of interpolation avoid locking phenomena, isogeometric models, like all displacement based formulations, suffer from this pathology, that arises from the coupling terms appearing in the strain energy. Membrane and shear locking were observed in plane beam models [30–33] and membrane and flexural locking in space rod models [10,34–36]. In [1,36] severe locking due to these interactions was found, even for high order interpolations. Raising the degree of the interpolating functions, locking was only slightly reduced but did not disappear. The same phenomenon had been observed by other researchers, who proposed different remedies. The discrete strain gap method and its extension to the isogeometric analysis by means of a collocation of the discrete strain gaps have been presented in [37,30], consistent interpolation and collocation method are presented in [31,38,39], reduced integration was used in [32] and B-bar formulations in [40,32–34,41].

In [26] it was shown that the implicit  $G^1$  continuous formulation yields much better results with respect to the locking pathologies, even though the phenomenon is still present, especially with reference to flexural locking. Furthermore, instabilities in the internal force distributions were observed, that reduced the accuracy of the solution. The aim of this work is to investigate the ability of a mixed formulation based on a B-bar  $L^2$  projection method for a  $G^1$  continuous space rod model to prevent the occurrence of locking, and consequently to improve the accuracy of the solution.

In [32] the authors compare several numerical strategies for the treatment of locking in plane rods, namely reduced integration, discrete strain gap, and B-bar strain projection method. They show that for coarse meshes the B-bar strain projection method produces solutions with greater accuracy than the other considered methods. From a numerical point of view both discrete strain gap and B-bar strain projection method produce a full stiffness matrix, for this reason in [42] a strategy for reducing the band-width of the modified stiffness matrix by means of a local least-square procedure has been proposed.

Accounting for these results, in this work a mixed approach is introduced in the  $G^1$  formulation, analogous to the one adopted in [33,34], leading to a B-bar type formulation. Using the multi patch approach with  $G^1$  continuity a full stiffness matrix is obtained only at the level of the patch while the global stiffness matrix has the same band-width of the stiffness matrix of a single patch, with great improvement in the computational cost.

In Section 2 the space rod model is briefly presented; in Section 3 the implicit  $G^1$  continuous model is summarized. The B-bar type formulation is implemented in Section 4, and it is used in the subsequent applications. Examples

presenting different forms of energy coupling are finally discussed, in order to investigate the performance of the formulation and its ability to avoid locking and to improve accuracy.

## 2. The Kirchhoff rod model

The model of a space Kirchhoff rod has been presented in [1,26]. In this section we will only recall the essential results useful for understanding the subsequent developments. The full derivation of the model can be found in the cited papers.

The geometry of the rod is defined by the couple  $(\Gamma, \mathfrak{E})$ , where  $\Gamma$  is a curve of  $\mathbb{R}^3$  having parametric equations  $\mathbf{p}(S) : \mathcal{A} \rightarrow \mathbb{R}^3$ ,  $\mathcal{A} = ]0, L_0[$ . In this way  $S$  is the arc length of the reference Lagrangian configuration;  $\mathfrak{E} = \{\hat{\mathbf{t}}, \hat{\mathbf{n}}, \hat{\mathbf{v}}\}$  is an orthogonal triad, with  $\hat{\mathbf{t}} = \frac{d\mathbf{p}}{dS} \frac{1}{\|\hat{\mathbf{t}}\|}$ ,  $\hat{\mathbf{t}} = \frac{d\mathbf{p}}{dS}$ , and  $\hat{\mathbf{n}}(S)$ ,  $\hat{\mathbf{v}}(S)$  are two director vectors orthogonal to  $\hat{\mathbf{t}}(S)$ .

The reference configuration, at time  $t = 0$ , is denoted by the index '0'. A generic configuration of the rod is defined by the centreline position  $\mathbf{p}(S) = \mathbf{p}_0(S) + \mathbf{u}(S)$ , and by the rotation operator  $\Omega$  of the internal triad,  $(\hat{\mathbf{t}}, \hat{\mathbf{n}}, \hat{\mathbf{v}}) = \Omega(\hat{\mathbf{t}}_0, \hat{\mathbf{n}}_0, \hat{\mathbf{v}}_0)$ .

Kirchhoff hypotheses require that, at any instant, the cross sectional axes be orthogonal to the tangent vector to the centreline, i.e.,

$$\hat{\mathbf{n}} \cdot \hat{\mathbf{t}} = 0 \quad \hat{\mathbf{v}} \cdot \hat{\mathbf{t}} = 0, \quad \forall(t, S). \quad (1)$$

From Eq. (1) it follows that the velocity of rotation  $\dot{\omega}$  of the intrinsic triad is given by

$$\begin{aligned} \dot{\omega}_n &= \dot{\hat{\mathbf{v}}} \cdot \hat{\mathbf{t}} = -\hat{\mathbf{v}} \cdot \dot{\hat{\mathbf{t}}} = -\hat{\mathbf{v}} \cdot \frac{d\dot{\mathbf{u}}}{dS} \frac{1}{\|\hat{\mathbf{t}}\|} \\ \dot{\omega}_v &= -\dot{\hat{\mathbf{n}}} \cdot \hat{\mathbf{t}} = \hat{\mathbf{n}} \cdot \dot{\hat{\mathbf{t}}} = \hat{\mathbf{n}} \cdot \frac{d\dot{\mathbf{u}}}{dS} \frac{1}{\|\hat{\mathbf{t}}\|} \end{aligned} \quad (2)$$

while the torsional velocity of rotation is

$$\dot{\omega}_t = \dot{\hat{\mathbf{n}}} \cdot \hat{\mathbf{v}} = \dot{\phi}. \quad (3)$$

Therefore the bending velocities of rotation are obtained as derivatives of the velocity of displacement.

Denoting by  $\varepsilon$  the axial strain, by  $\chi_n, \chi_v$  the bending curvatures and by  $\chi_t$  the torsional curvature, the compatibility equations for the velocities of the strains are given by the following expressions:

$$\begin{aligned} \dot{\varepsilon} &= \frac{d\dot{\mathbf{u}}}{dS} \cdot \hat{\mathbf{t}} \\ \dot{\chi}_n &= \left[ -\frac{d^2\dot{\mathbf{u}}}{dS^2} + \dot{\phi} \left( \hat{\mathbf{t}} \times \frac{d\hat{\mathbf{t}}}{dS} \right) \right] \cdot \hat{\mathbf{v}} \\ \dot{\chi}_v &= - \left[ -\frac{d^2\dot{\mathbf{u}}}{dS^2} + \dot{\phi} \left( \hat{\mathbf{t}} \times \frac{d\hat{\mathbf{t}}}{dS} \right) \right] \cdot \hat{\mathbf{n}} \\ \dot{\chi}_t &= \frac{d\dot{\phi}}{dS} + \frac{1}{\|\hat{\mathbf{t}}\|^2} \frac{d\dot{\mathbf{u}}}{dS} \cdot \left( \hat{\mathbf{t}} \times \frac{d\hat{\mathbf{t}}}{dS} \right) \end{aligned} \quad (4)$$

with  $\frac{d^2\dot{\mathbf{u}}}{dS^2} = \|\hat{\mathbf{t}}\| \frac{d}{dS} \left( \frac{1}{\|\hat{\mathbf{t}}\|} \frac{d\dot{\mathbf{u}}}{dS} \right)$ , while  $\left( \hat{\mathbf{t}} \times \frac{d\hat{\mathbf{t}}}{dS} \right) = \frac{1}{\|\hat{\mathbf{t}}\|} (\chi_n \hat{\mathbf{n}} + \chi_v \hat{\mathbf{v}})$  is the curvature of the centreline.

In this work we restrict ourselves to infinitesimal deformations, so that the expressions (4) can be formally used for the infinitesimal strain measures, using as geometry of the rod the reference initial configuration. For the infinitesimal strains the same symbols as in (4) will be adopted, removing the dots.

The weak form of the equilibrium equations is given by the principle of virtual power, that is, for any admissible velocity field  $\dot{\mathbf{u}}, \dot{\phi}$  the following equality must hold:

$$\begin{aligned} &\int_{L_0} (N \dot{\varepsilon}(\dot{\mathbf{u}}, \dot{\phi}) + M_n \dot{\chi}_n(\dot{\mathbf{u}}, \dot{\phi}) + M_v \dot{\chi}_v(\dot{\mathbf{u}}, \dot{\phi}) + M_t \dot{\chi}_t(\dot{\mathbf{u}}, \dot{\phi})) dS \\ &= \int_{L_0} \mathbf{1} \cdot \dot{\mathbf{u}} dS + \mathbf{F}_0 \cdot \dot{\mathbf{u}}_0 + \mathbf{F}_L \cdot \dot{\mathbf{u}}_L + \mathbf{M}_0 \cdot \dot{\omega}_0 + \mathbf{M}_L \cdot \dot{\omega}_L. \end{aligned} \quad (5)$$

In (5)  $\mathbf{I}(S)$  is the external load vector and  $\mathbf{F}_0, \mathbf{F}_L, \mathbf{M}_0, \mathbf{M}_L$  are point forces and couples applied at the ends of the rod. For small strains the internal forces are linearly related to the strains:

$$\begin{aligned} N &= EA \varepsilon & M_t &= GJ_t (\chi_t - \chi_{t0}) \\ M_n &= EI_n (\chi_n - \chi_{n0}) & M_v &= EI_v (\chi_v - \chi_{v0}), \end{aligned} \quad (6)$$

where  $\chi_{n0}, \chi_{v0}, \chi_{t0}$  are the initial curvatures of the rod axis.

The present formulation applies to a generic incremental step if the geometric stiffness matrix is disregarded. The general formulation for non linear Kirchhoff rods can be found in [2] (see also [43,44] for planar beams).

### 3. The implicit $G^1$ continuous numerical model

A B-spline interpolation of the variables  $(\mathbf{u}, \phi)$  is introduced, so that

$$\begin{aligned} \mathbf{p}(\lambda) &= \sum_{i=1}^n b_i^p \mathbf{P}_i \\ \phi(\lambda) &= \sum_{i=1}^n b_i^p \Phi_i \end{aligned} \quad \lambda \in (0, 1). \quad (7)$$

Here  $b_i^p(\lambda)$  are  $n$  B-spline basis functions of degree  $p$ , with  $n = p + 1 + k$ , with  $k$  the number of internal knots in the knot span vector

$$\Xi = \{ \underbrace{0, \dots, 0}_{p+1}, \underbrace{\lambda_1, \dots, \lambda_k}_k, \underbrace{1, \dots, 1}_{p+1} \} \quad (8)$$

that globally defines a patch in the parametric domain. The interval  $(\lambda_i, \lambda_{i+1})$  is called a section or an element. If there is no internal knot, the basis functions reduce to the Bernstein basis polynomials.

$\mathbf{P}_i$  are the position vectors of the control points of the rod axis, that control the shape of the curve. Similarly  $\Phi_i$  are the control points for the interpolation of the torsion angle.

Collecting the degrees of freedom in the vector  $\mathbf{q}$

$$\mathbf{q} = \{ \underbrace{\mathbf{P}_1, \Phi_1, \mathbf{P}_2, \Phi_2, \dots, \mathbf{P}_{n-1}, \Phi_{n-1}}_{\mathbf{q}_{1,2}}, \underbrace{\mathbf{P}_n, \Phi_n}_{\mathbf{q}_{n-1,n}} \} \quad (9)$$

the configuration of the rod is given by the interpolation

$$\{\mathbf{p}(\lambda), \phi(\lambda)\} = \mathbb{M}\mathbf{q} \quad (10)$$

with

$$\mathbb{M} = \begin{pmatrix} b_1^p & 0 & 0 & 0 & b_n^p & 0 & 0 & 0 \\ 0 & b_1^p & 0 & 0 & 0 & b_n^p & 0 & 0 \\ 0 & 0 & b_1^p & 0 & \dots & 0 & 0 & b_n^p \\ 0 & 0 & 0 & b_1^p & 0 & 0 & 0 & b_n^p \end{pmatrix}. \quad (11)$$

Since an open knot vector has been used, the B-spline interpolation is not interpolatory except at the end points of the patch. Therefore only  $C^0$  continuity is obtained, and in general additional constraints have to be added for the end rotations in order to fulfil the boundary conditions.

Two curves meet with  $C^1$  parametric continuity if the parametric tangents,  $\mathbf{t} = \frac{d\mathbf{p}}{d\lambda}$ , are the same at the joint; so that, under a generic re-parametrization of the curves the parametric continuity is destroyed. Conversely, two curves meet with  $G^1$  geometric continuity if the unit tangents, are the same at the joint. The geometric continuity is independent under a generic re-parametrization of the curves, for details see [45] and [46].

A  $G^1$  implicit formulation for space rods has been proposed in [26] and [35], introducing the end rotations as degrees of freedom by means of a change of basis for the control variables of the B-spline interpolation of the centroid curve, analogously to the Hermitian interpolation concept. For the convenience of the reader the method is summarized in the following.

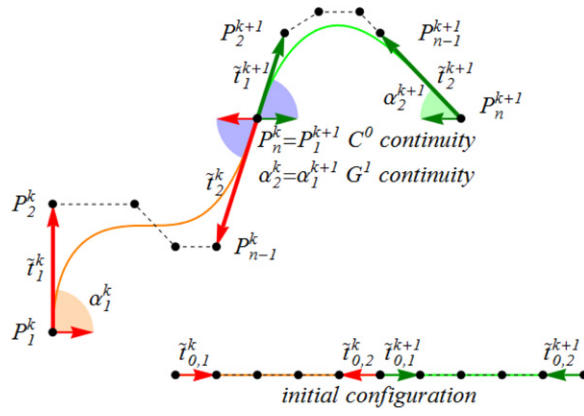


Fig. 1. Geometric representation of the  $G^1$  continuity as implicit constraint on the rotations at the joints of the elements.

The coordinate transformation is performed mapping the second,  $\mathbf{P}_2$ , and the second-last,  $\mathbf{P}_{n-1}$ , control points of each patch by means of the spatial rotations and the deformation of the end control segments vectors  $\tilde{\mathbf{t}}_{0,1}$  and  $\tilde{\mathbf{t}}_{0,2}$  as follows (see Fig. 1)

$$\mathbf{P}_2 = \mathbf{P}_1 + \rho_1 \tilde{\mathbf{R}}_1 \tilde{\mathbf{t}}_{0,1}, \quad \mathbf{P}_{n-1} = \mathbf{P}_n + \rho_2 \tilde{\mathbf{R}}_2 \tilde{\mathbf{t}}_{0,2}, \quad (12)$$

where  $\tilde{\mathbf{R}}_1$  and  $\tilde{\mathbf{R}}_2$  are spatial rotation operators,

$$\tilde{\mathbf{t}}_{0,1} = \mathbf{P}_{0,2} - \mathbf{P}_{0,1}, \quad \tilde{\mathbf{t}}_{0,2} = \mathbf{P}_{0,n-1} - \mathbf{P}_{0,n}, \quad (13)$$

and the scalars  $\rho_1$  and  $\rho_2$  are the relative changes in the lengths of these vectors, i.e.

$$\rho_1 = \frac{\|\mathbf{P}_2 - \mathbf{P}_1\|}{\|\mathbf{P}_{0,2} - \mathbf{P}_{0,1}\|} = \frac{\|\tilde{\mathbf{t}}_1\|}{\|\tilde{\mathbf{t}}_{0,1}\|}, \quad \rho_2 = \frac{\|\mathbf{P}_{n-1} - \mathbf{P}_n\|}{\|\mathbf{P}_{0,n-1} - \mathbf{P}_{0,n}\|} = \frac{\|\tilde{\mathbf{t}}_2\|}{\|\tilde{\mathbf{t}}_{0,2}\|}. \quad (14)$$

The  $G^1$  parametric continuity is thus obtained equating the unit director  $\hat{\mathbf{t}}_1^{k+1}$  at the first end of the  $k+1$  patch with the unit director  $\hat{\mathbf{t}}_2^k$  at the last end of the previous patch, i.e.

$$\frac{\tilde{\mathbf{t}}_1^{k+1}}{\|\tilde{\mathbf{t}}_1^{k+1}\|} = -\frac{\tilde{\mathbf{t}}_2^k}{\|\tilde{\mathbf{t}}_2^k\|}. \quad (15)$$

Recalling that  $\hat{\mathbf{t}}_i^k = \tilde{\mathbf{R}}_i^k \hat{\mathbf{t}}_{0,i}^k$ , Eq. (15) means that  $\tilde{\mathbf{R}}_1^{k+1} \hat{\mathbf{t}}_{0,1}^{k+1} = -\tilde{\mathbf{R}}_2^k \hat{\mathbf{t}}_{0,2}^k$ , and, since  $\hat{\mathbf{t}}_{0,2}^k = -\hat{\mathbf{t}}_{0,1}^{k+1}$  the  $G^1$  parametric continuity implies that  $\tilde{\mathbf{R}}_1^{k+1} = \tilde{\mathbf{R}}_2^k$ .

In terms of velocity equality (15) leads to

$$\dot{\hat{\mathbf{t}}}_2^k = -\dot{\hat{\mathbf{t}}}_1^{k+1} \quad (16)$$

or, introducing the velocities of rotation of the two end points,  $\hat{\omega}_2^k, \hat{\omega}_1^{k+1}$

$$\hat{\omega}_1^{k+1} \times \hat{\mathbf{t}}_1^{k+1} = -\hat{\omega}_2^k \times \hat{\mathbf{t}}_2^k \quad (17)$$

so that the constraint is fulfilled if the velocities of rotation of the ends of the patches,  $\hat{\omega}_1^{k+1}, \hat{\omega}_2^k$  are equal. In the hypothesis of small deformations the same result holds for the infinitesimal rotations. The end rotations and elongations are used as degrees of freedom and are collected in the vector  $\mathbf{y}$  defined as

$$\mathbf{y} = \underbrace{\{\mathbf{P}_1, \omega_1, \rho_1, \Phi_2; \mathbf{P}_3, \Phi_3, \dots, \mathbf{P}_{n-2}, \Phi_{n-2}; \Phi_{n-1}, \rho_2, \mathbf{P}_n, \omega_2\}}_{\mathbf{y}_{1,2}} \quad (18)$$

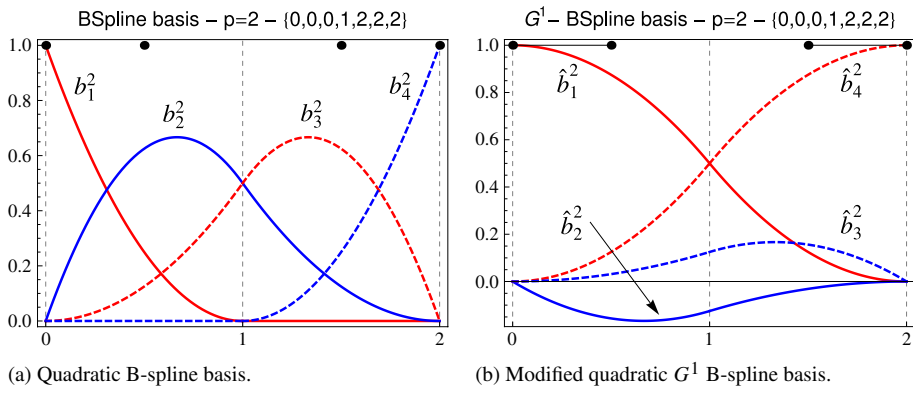


Fig. 2. Standard quadratic B-spline basis with one internal knot (on the left) and corresponding  $G^1$ -transformed B-spline basis functions (on the right).

that is related to the original degrees of freedom  $\mathbf{q}$  through a linear transformation, that actually involves only the first two and the last two control points. With the notations  $\mathbf{0}_3 = \{0, 0, 0\}$  and  $\mathbf{I}_3 =$  identity  $3 \times 3$  matrix, it is:

$$\mathbf{q}_{1,2} = \mathbb{E}_1 \mathbf{y}_{1,2}, \quad \mathbb{E}_1 = - \begin{pmatrix} \mathbf{I}_3 & \mathbf{0}_3 \otimes \mathbf{0}_3 & \mathbf{0}_3^T & \mathbf{0}_3^T \\ \mathbf{0}_3 & \hat{\mathbf{t}}_1 \cdot & 0 & 0 \\ \mathbf{I}_3 & -\tilde{\mathbf{t}}_1 \times & \frac{\tilde{\mathbf{t}}_1}{\rho_1} & \mathbf{0}_3^T \\ \mathbf{0}_3 & \mathbf{0}_3 & 0 & 1 \end{pmatrix}, \quad (19)$$

and

$$\mathbf{q}_{n-1,n} = \mathbb{E}_2 \mathbf{y}_{n-1,n}, \quad \mathbb{E}_2 = - \begin{pmatrix} \mathbf{0}_3^T & \frac{\tilde{\mathbf{t}}_2}{\rho_2} & \mathbf{I}_3 & -\tilde{\mathbf{t}}_2 \times \\ 1 & 0 & \mathbf{0}_3 & \mathbf{0}_3 \\ \mathbf{0}_3^T & \mathbf{0}_3^T & \mathbf{I}_3 & \mathbf{0}_3 \otimes \mathbf{0}_3 \\ 0 & 0 & \mathbf{0}_3 & \hat{\mathbf{t}}_2 \cdot \end{pmatrix}. \quad (20)$$

Fig. 2 presents the modified interpolation functions  $\hat{b}_i^2$  for  $p = 2$  obtained with the transformations (19), (20). Notice that in the case  $p = 2$  it is necessary to introduce at least one internal knot in the original B-spline basis in order to have 4 control points.

In the case  $p = 3$  the transformation leads to cubic Hermitian polynomials. Please be aware that the element so obtained is not equivalent to a standard Hermitian element like the one proposed by Armero and Valverde [34], who employ cubic interpolation for the bending deformation but linear interpolation for the axial displacement.

#### 4. Mixed formulation

Displacement based formulation for thin structural models is known to present membrane and/or shear locking, and locking due to bending and torsional interaction is present in curved space elements [10].

In [26] the rate of convergence of a single patch B-spline interpolation with increasing number of internal knots was compared with the rate of convergence of the same problem modelled with a  $G^1$  continuous multi-patch approach. It was found that the latter approach has the same rate of convergence as the single patch interpolation with  $k$ -refinement, but a lower accuracy. However, it was also found that B-spline interpolations for a space Kirchhoff–Love rod suffer from strain locking. Increasing the degree of the interpolation, locking decreases but does not disappear, since it is intrinsically linked to the kinematic model. Similar conclusions hold for space rods modelled with  $G^1$  continuous multi-patches. Locking was still present, although with reduced intensity, compare for instance figures 8 and 13 of [26].

In the present section a formulation for a  $G^1$  continuous interpolation of Kirchhoff–Love space rods able to suppress locking is presented. Since the bending curvatures depend on both the second derivatives of the displacements

and the torsional rotation, and the torsional curvature depends on the first derivatives both of the displacements and of the torsional rotation a consistent interpolation method is not applicable. Therefore a mixed formulation leading to a B-bar method is used instead.

B-bar methods, commonly based on the Assumed Strain Method, for which the discrete strain measures are modified, are derived from the mixed Hu–Washizu variational principle [33]. The discrete strains are projected onto a basis of lower dimension in order to relax the kinematic constraints related to the mismatch introduced by the displacement interpolations. A slightly different method is used here, that stems out from the Hellinger–Reissner variational principle. Independent interpolations are introduced for the internal forces dual of the strain measures. An  $L^2$  projection onto bases of lower dimensions than those used for interpolating the displacements is used. As it will be shown, in the case of linear behaviour the present procedure is equivalent to the B-bar method based on Assumed Strains. Equivalence between enhanced assumed strain method and assumed stress hybrid method was established by Ye and Lee [47].

The Assumed Strain Method (ASM) for isogeometric analysis was first proposed in [40] for the analysis of nearly incompressible 2D elasticity (for avoiding volumetric locking). Recently Bouclier et al. [32] have examined membrane and shear locking pathologies in 2D polar rods; they project the strain measures on a lower order polynomial space letting unchanged the knot vector and show that this kind of B-bar approach is particularly convenient for the  $k$ -refinement of isogeometric analysis.

However, due to the necessity of inverting a Gram matrix, a mixed formulation based on ASM in the isogeometric framework with high order inter element continuity leads to a full modified global stiffness matrix, as highlighted in [42,30]. On the contrary, in a multi-patch approach with low interpatch continuity, the effect of the inversion of the Gram matrix is confined only to the patch level, so that the global stiffness matrix is not full. Therefore in this work we propose a B-bar formulation for  $G^1$  multi-patch interpolations and investigate its ability to avoid locking phenomena and its effect on the rate of convergence of the method under refinement operations.

The Hellinger–Reissner mixed functional for a linear elastic Kirchhoff rod is

$$\begin{aligned} \Pi(\mathbf{u}, \phi, N, M_n, M_v, M_t) = & -\frac{1}{2} \int_{L_0} \left( \frac{N^2}{EA} + \frac{M_v^2}{EI_v} + \frac{M_n^2}{EI_n} + \frac{M_t^2}{GJ_t} \right) dS \\ & + \int_{L_0} (N\varepsilon(\mathbf{u}) + M_n\chi_n(\mathbf{u}, \phi) + M_v\chi_v(\mathbf{u}, \phi) + M_t\chi_t(\mathbf{u}, \phi)) dS - \int_{L_0} \mathbf{1} \cdot \mathbf{u} dS, \end{aligned} \quad (21)$$

where the strain measures are given as function of the degrees of freedom by expressions analogous to Eqs. (4) (small strains are considered). For convenience only the distributed load has been considered. The variation with respect to the internal forces gives the compatibility equations (a tilde indicates variations):

$$\begin{aligned} \int_{L_0} \tilde{N} \left( \frac{N}{EA} - \varepsilon(\mathbf{u}) \right) dS &= 0 \quad \forall \tilde{N} \\ \int_{L_0} \tilde{M}_n \left( \frac{M_n}{EI_n} - \chi_n(\mathbf{u}, \phi) \right) dS &= 0 \quad \forall \tilde{M}_n \\ \int_{L_0} \tilde{M}_v \left( \frac{M_v}{EI_v} - \chi_v(\mathbf{u}, \phi) \right) dS &= 0 \quad \forall \tilde{M}_v \\ \int_{L_0} \tilde{M}_t \left( \frac{M_t}{GJ_t} - \chi_t(\mathbf{u}, \phi) \right) dS &= 0 \quad \forall \tilde{M}_t. \end{aligned} \quad (22)$$

Introducing the interpolation (10) the strains are given by

$$\varepsilon = \mathbf{B}_\varepsilon \mathbf{y}, \quad \chi_t = \mathbf{B}_{\chi_t} \mathbf{y}, \quad \chi_n = \mathbf{B}_{\chi_n} \mathbf{y}, \quad \chi_v = \mathbf{B}_{\chi_v} \mathbf{y}. \quad (23)$$

The expressions for the deformation matrices indicated in Eqs. (23) are reported in the Appendix. The following interpolations are assumed for the stress resultants

$$N = (\mathbf{b}^{p-1})^T \mathbf{n}_a \quad M_t = (\mathbf{b}^{p-1})^T \mathbf{m}_t \quad (24)$$

and

$$M_n = (\mathbf{b}^{p-2})^T \mathbf{m}_n \quad M_v = (\mathbf{b}^{p-2})^T \mathbf{m}_v \quad (25)$$

where  $\mathbf{n}_a, \mathbf{m}_t, \mathbf{m}_n, \mathbf{m}_v$  are vectors collecting the control values of the interpolation of the internal forces, and  $(\mathbf{b}^{p-1}), (\mathbf{b}^{p-2})$  are row matrices containing the B-spline basis functions of degree  $p - 1, p - 2$  respectively. The B-spline bases  $b_i^p, b_i^{p-1}, b_i^{p-2}$  use the same element span, that is their knot vectors have the same internal knots.

Substituting the interpolations (24) and (25) in the compatibility equations (22), it is obtained

$$\begin{aligned} & \left( \frac{1}{EA} \int_{L_0} (\mathbf{b}^{p-1})^T (\mathbf{b}^{p-1}) dS \mathbf{n}_a - \int_{L_0} (\mathbf{b}^{p-1})^T \mathbf{B}_\varepsilon dS \mathbf{y} \right) \cdot \tilde{\mathbf{n}}_a = 0, \quad \forall \tilde{\mathbf{n}}_a \\ & \left( \frac{1}{GJ_t} \int_{L_0} (\mathbf{b}^{p-1})^T (\mathbf{b}^{p-1}) dS \mathbf{m}_t - \int_{L_0} (\mathbf{b}^{p-1})^T \mathbf{B}_{\chi_t} dS \mathbf{y} \right) \cdot \tilde{\mathbf{m}}_t = 0, \quad \forall \tilde{\mathbf{n}}_a \\ & \left( \frac{1}{EI_n} \int_{L_0} (\mathbf{b}^{p-2})^T (\mathbf{b}^{p-2}) dS \mathbf{m}_n - \int_{L_0} (\mathbf{b}^{p-2})^T \mathbf{B}_{\chi_n} dS \mathbf{y} \right) \cdot \tilde{\mathbf{m}}_n = 0, \quad \forall \tilde{\mathbf{m}}_n \\ & \left( \frac{1}{EI_v} \int_{L_0} (\mathbf{b}^{p-2})^T (\mathbf{b}^{p-2}) dS \mathbf{m}_v - \int_{L_0} (\mathbf{b}^{p-2})^T \mathbf{B}_{\chi_v} dS \mathbf{y} \right) \cdot \tilde{\mathbf{m}}_v = 0, \quad \forall \tilde{\mathbf{m}}_v. \end{aligned} \quad (26)$$

These equations are solved with respect to the stress control variables:

$$\begin{aligned} \mathbf{n}_a &= EA \bar{\mathbf{G}}^{-1} \mathbb{E}_\varepsilon \mathbf{y}, \\ \mathbf{m}_t &= GJ_t \bar{\mathbf{G}}^{-1} \mathbb{E}_{\chi_t} \mathbf{y}, \\ \mathbf{m}_n &= EI_n \bar{\mathbf{G}}^{-1} \mathbb{E}_{\chi_n} \mathbf{y}, \\ \mathbf{m}_v &= EI_v \bar{\mathbf{G}}^{-1} \mathbb{E}_{\chi_v} \mathbf{y}. \end{aligned} \quad (27)$$

The variation of the functional (21) with respect to the displacement degrees of freedom gives the discrete equilibrium equations

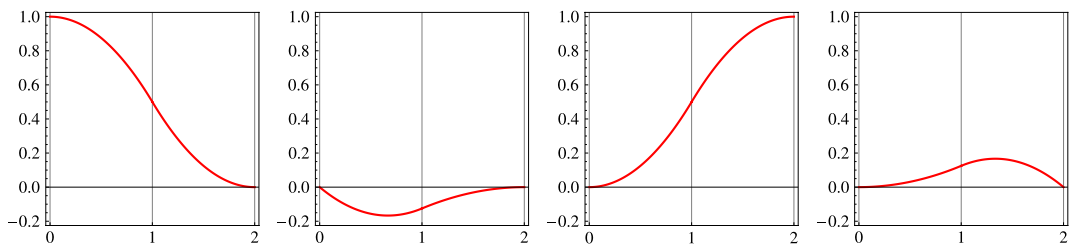
$$\int_{L_0} (\mathbf{B}_\varepsilon^T N + \mathbf{B}_{\chi_n} M_n + \mathbf{B}_{\chi_v} M_v + \mathbf{B}_{\chi_t} M_t) dS \cdot \tilde{\mathbf{y}} - \int_{L_0} \mathbb{M}^T \mathbf{I} dS \cdot \tilde{\mathbf{y}} = \mathbf{0}, \quad \forall \tilde{\mathbf{y}}. \quad (28)$$

Using the stress interpolations (24) and (25) and the results (27) in the equilibrium equations one has the final form

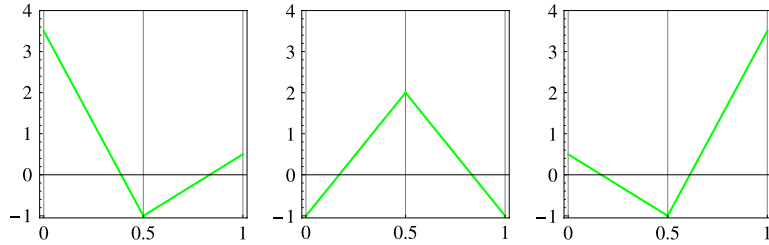
$$\left[ EA \left( \mathbb{E}_\varepsilon^T \bar{\mathbf{G}}^{-1} \mathbb{E}_\varepsilon \right) + EI_v \left( \mathbb{E}_{\chi_v}^T \bar{\mathbf{G}}^{-1} \mathbb{E}_{\chi_v} \right) + EI_n \left( \mathbb{E}_{\chi_n}^T \bar{\mathbf{G}}^{-1} \mathbb{E}_{\chi_n} \right) + GJ_t \left( \mathbb{E}_{\chi_t}^T \bar{\mathbf{G}}^{-1} \mathbb{E}_{\chi_t} \right) \right] \mathbf{y} = \mathbf{F}. \quad (29)$$

The matrices  $\bar{\mathbf{G}}$  and  $\bar{\bar{\mathbf{G}}}$  are the *Gram* matrices for the reduced B-spline bases. In this way the stiffness operator is obtained in terms of the configuration variables only. The quadrature is performed at level of each non null section considering  $p + 1$  *Gauss-Lobatto* points. Gauss-Legendre quadrature could be used equivalently, but the former has been preferred in consideration of future extensions to material non-linearities.

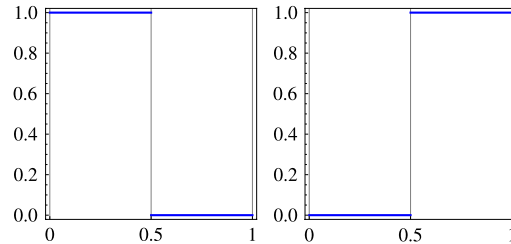
The procedure illustrated is convenient for  $k$ -refinement, since adding internal knots does not alter the structure of the stiffness matrix, see [32]. In Figs. 3 and 4 are illustrated the interpolating B-spline for the displacements and the



(a) Second degree modified  $G^1$  B-spline basis functions,  $\hat{b}_j^2$ , with knot vector  $\Xi = \{0, 0, 0, 1, 2, 2, 2\}$ .



(b) First order B-spline basis functions,  $b^{1,i}$ , used to interpolate the axial force and the torsional moment, with knot vector  $\Xi = \{0, 0, 0, 1, 2, 2, 2\}$ .



(c) Zero order B-spline basis functions used to interpolate the bending moments, with knot vector  $\Xi = \{0, 0, 0, 1, 2, 2, 2\}$ .

Fig. 3. Second degree interpolating basis functions with one internal knot, (the knot vector  $\Xi = \{0, 0, 0, 1, 2, 2, 2\}$  is the same for all interpolating spaces).

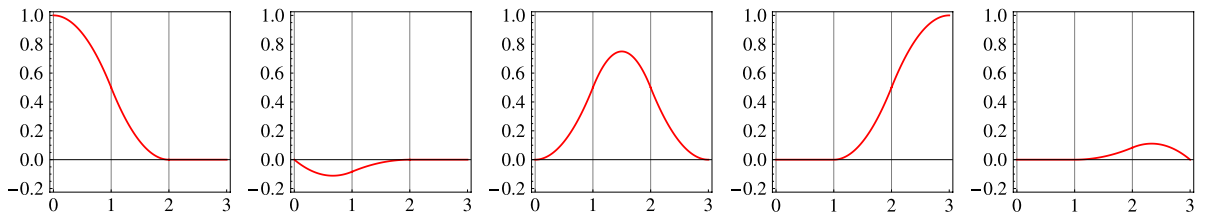
stress resultants, for a quadratic interpolation with knot vectors  $\Xi = \{0, 0, 0, 1, 2, 2, 2\}$  and  $\Xi = \{0, 0, 0, 1, 2, 3, 3, 3\}$  respectively. In this case the *Gram* matrix  $\bar{\mathbf{G}}$  reduces to the identity matrix.

## 5. Numerical investigation

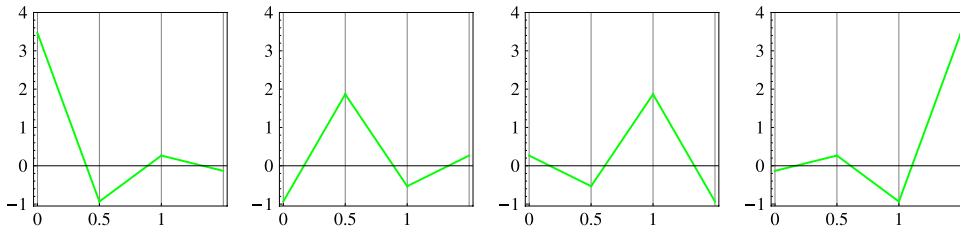
The proposed  $G^1$  continuous formulation encourages the use of low order elements, therefore the numerical applications are focused on second and third order interpolations. The proposed mixed formulation permits a strong reduction of locking, without the need of increasing the order of the interpolation with the related computational costs.

In the following simple academic examples are considered for testing the efficiency of the method. The first example concerns a case that presents membrane locking; the second example considers an out of plane arch deformation where flexural locking arises. Finally curved elements with discontinuities on the geometry or on the internal forces are considered. The last examples will allow to investigate the ability of the proposed method to avoid instabilities in the internal forces when sharp discontinuities are present.

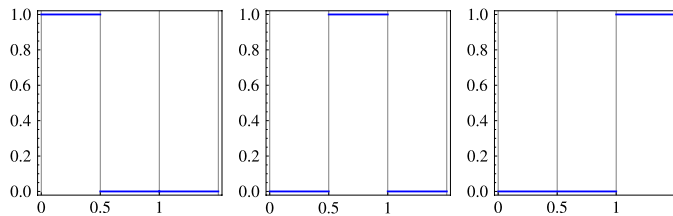
In all cases it has been evaluated how the error depends on the thickness ratio of the rod, under patch refinement, that is, increasing the number of patches employed, joined with  $G^1$  continuity, with no internal knot (except in the case  $p = 2$  as observed at the end of Section 3).



(a) Second degree modified  $G^1$  B-spline basis functions,  $\hat{b}_j^2$ , with knot vector  $\Xi = \{0, 0, 0, 1, 2, 3, 3, 3\}$ .



(b) First order B-spline basis functions,  $b^{1,i}$ , used to interpolate the axial force and the torsional moment, with knot vector  $\Xi = \{0, 0, 0, 1, 2, 3, 3, 3\}$ .



(c) Zero order B-spline basis functions used to interpolate the bending moments, with knot vector  $\Xi = \{0, 0, 0, 1, 2, 3, 3, 3\}$ .

Fig. 4. Second degree interpolating basis functions with two internal knots, (the knot vector  $\Xi = \{0, 0, 0, 1, 2, 3, 3, 3\}$  is the same for all interpolation spaces).

### 5.1. Membrane locking: 2D arch with a point force at the free end

In this example is considered a 2D cantilever circular arch loaded at the tip by a vertical force  $\mathbf{F} = \{0, -1, 0\}$ , (kN). The radius of the centroid curve is  $R = 1$  (m) the section is rectangular with  $h_n = 0.1$ , the thickness  $h_v$  is variable,  $\hat{\mathbf{n}}(S) = \mathbf{e}_z$ ,  $\hat{\mathbf{v}} = \hat{\mathbf{t}} \times \mathbf{e}_z$  and  $E = 2.0 * 10^8$  (kN/m<sup>2</sup>). See Fig. 5 for the geometry.

For a displacement based model the solution is affected by membrane locking. This can be detected from Fig. 6, related to a  $G^1$  continuous formulation, that shows the relative error in the  $L^2$ -norm for the  $u_y$  displacement component obtained subdividing the arch in five patches for different polynomial degrees  $p = 2, 3, 4$  and for different values of the aspect ratio  $h_v/R$ . The  $L^2$  error is strongly dependent on the aspect ratio of the arch, especially for the lower order polynomial interpolations, where the error reaches 100%. Increasing the order of the interpolation this dependence is reduced but is still present, due to membrane locking. Using a B-spline single patch formulation, the dependence of the error on the aspect ratio is still greater, as was observed in [26]. The reduction of the interpatch continuity improves the situation, but does not eliminate the locking phenomena.

#### 5.1.1. Second degree polynomial interpolation

In this paragraph each patch is interpolated with quadratic polynomials, with an internal knot at  $\lambda = 0.5$  necessary for guaranteeing the  $G^1$  continuity, as explained at the end of Section 3. The relative error in  $L^2$ -norm for the displacement component  $u_y$  is plotted in Fig. 7(a) for different values of the thickness ratio  $R/h_v$ . On the horizontal axis is reported the number of control points used, that are increased dividing the arch into more and more patches. The number of control points is closely related to the element size, since uniform knot vectors have been used. A similar method of plotting the results has been adopted in [31]. The accuracy of the solution strongly decreases as

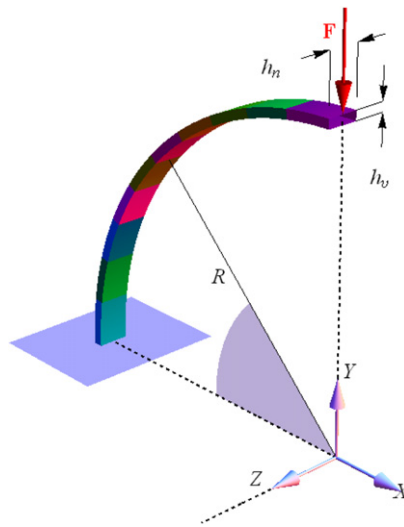


Fig. 5. 2D cantilever arch with a point force at the free end.

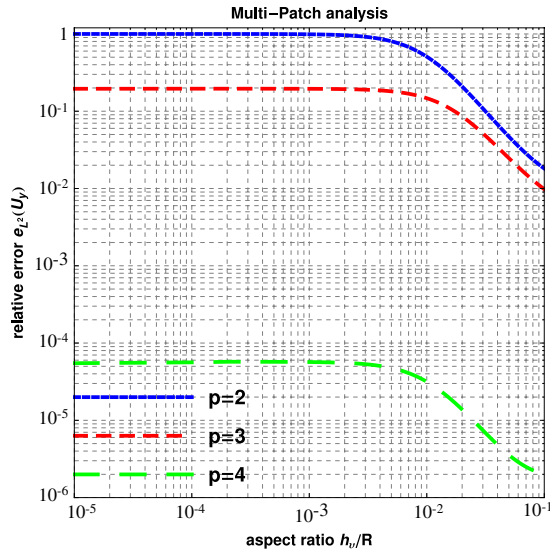


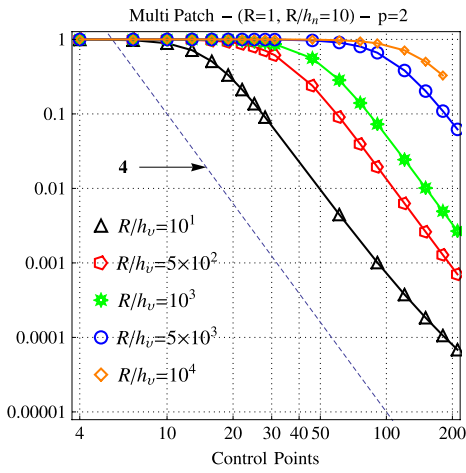
Fig. 6. 2D arch. Influence of the aspect ratio  $h_v/R$  on the solution for a fixed mesh with a displacement based  $G^1$  continuous formulation.

the slenderness parameter  $R/h_v$  increases. From the figure a super convergent asymptotic rate can be observed, with respect to the optimal rate  $p + 1$ , no matter what the thickness ratio is.

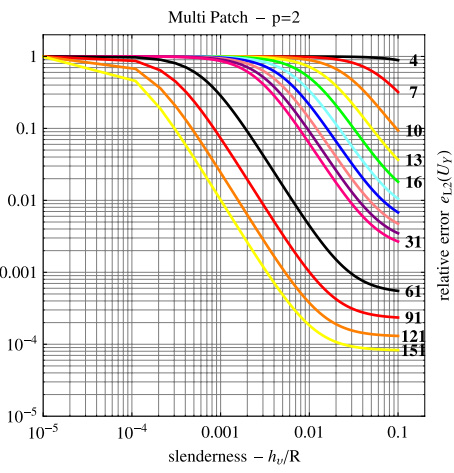
The same results are replotted in Fig. 7(b) against the thickness ratio. Each curve refers in this case to a different discretization, the numbers next to the curves indicate the number of control points used for the interpolation of the arch. The influence of the thickness ratio on the accuracy of the solution is apparent. Notice that the error reaches 100% for the most slender arch.

The same analysis has been repeated using the mixed formulation described in Section 4. Figs. 8(a) and 8(b) refer again to the relative error in  $L^2$  norm for the displacement component  $u_y$  and have to be compared with Figs. 7(a) and 7(b) obtained for the displacement based solution. Two observations can be made: the rate of convergence is sub-optimal (does not reach  $p + 1$ ), but the accuracy level of the solution is independent on the thickness ratio ( $R/h_v$ ).

In this example no discontinuity is present for the internal forces, differently from the examples presented in Section 5.3. Therefore the example can be used for comparing the accuracy of the multipatch solution with the accuracy of the single patch solution, in the case the mixed formulation is employed. When in the multi-patch approach

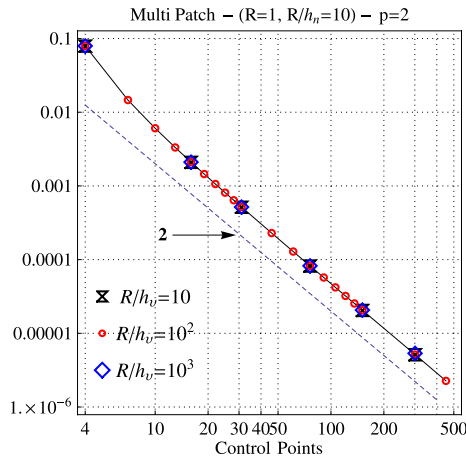


(a) Relative error in  $L^2$ -norm of  $u_y$  as function of the number of control points for different thickness ratios  $R/h_v$ .

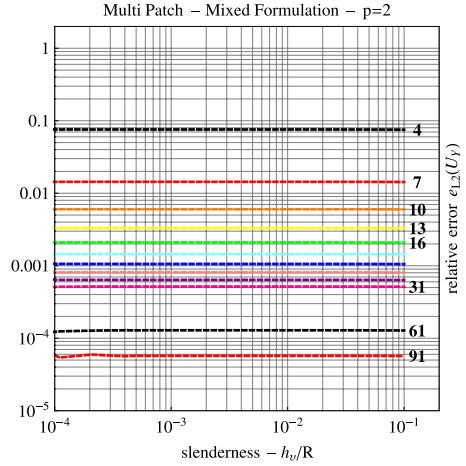


(b) Relative error in  $L^2$ -norm of  $u_y$  as function of the thickness ratio for different mesh levels, (the labels next to the curves are the number of control points used).

Fig. 7. 2D arch. Displacement based formulation with  $G^1$  continuity for second degree polynomial interpolation.



(a) Relative error in  $L^2$ -norm of  $u_y$  as function of the number of control points for different thickness ratios  $R/h_v$ . Only a subset of the results have been reported for clearness.

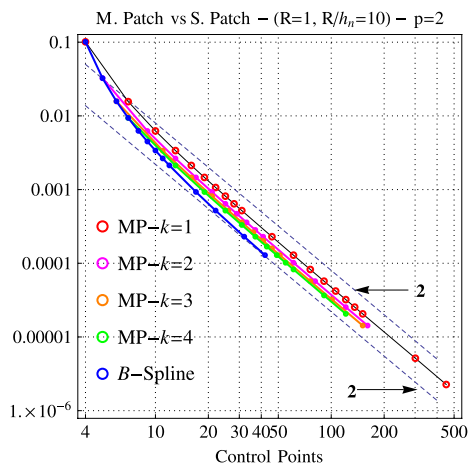


(b) Relative error in  $L^2$ -norm of  $u_y$  as function of the thickness ratio for different mesh levels, (the labels next to the curves are the number of control points used).

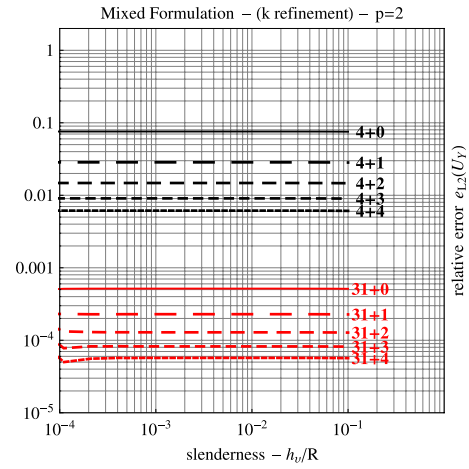
Fig. 8. 2D arch. Mixed formulation with  $G^1$  continuity for second degree polynomial interpolation.

the number of internal knots for each patch is increased the accuracy of the solution improves, tending towards the accuracy of the single patch B-spline solution (see Fig. 9(a), where the relative error for a fixed aspect ratio  $R/h_v = 10$  is plotted against the number of control points for different multi patch second order elements with increasing number of the internal knots). For all the discretizations used, however, the error is independent from the thickness ratio (Fig. 9(b)), confirming the absence of locking in this case.

Notice however that the  $G^1$  multi-patch approach has a great advantage with respect to the single patch solution, since the bandwidth of the stiffness matrix, that is full in the latter case, reduces to the number of degrees of freedom of the patch, thus improving the computational efficiency.

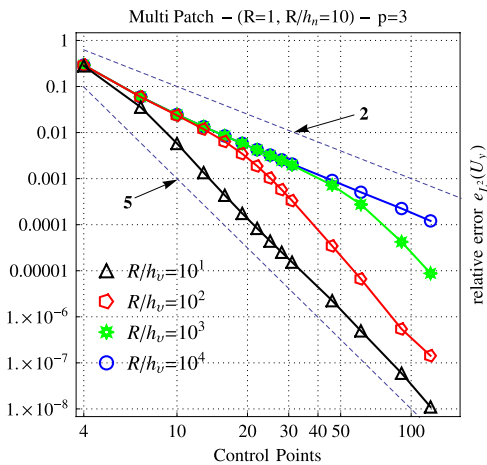


(a) Relative error in  $L^2$ -norm of  $u_y$  as function of the number of control points for different multi patch elements obtained increasing the number of internal knots.

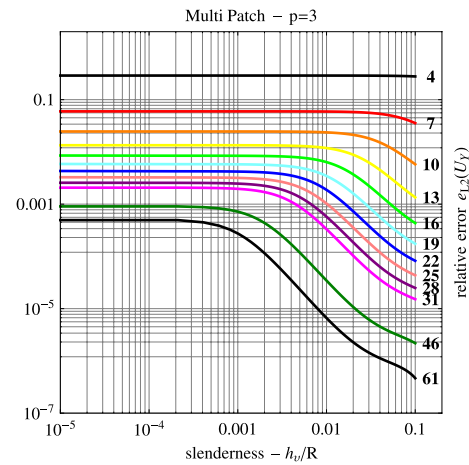


(b) Relative error in  $L^2$ -norm of  $u_y$  as function of the thickness ratios. The lines refer to discretizations with different number of patches and increasing number of internal knots.

Fig. 9. 2D arch. Mixed formulation with  $G^1$  continuity for second degree polynomial interpolation. Multi-patch formulation with increasing number of internal knots.



(a) Relative error in  $L^2$ -norm of  $u_y$  as function of the number of control points for different thickness ratios  $R/h_v$ .



(b) Relative error in  $L^2$ -norm of  $u_y$  as function of the thickness ratio for different mesh levels, (the labels next to the curves are the number of control points used).

Fig. 10. 2D arch. Displacement based formulation with  $G^1$  continuity for third degree polynomial Bezier's interpolation.

### 5.1.2. Third degree polynomial interpolation

The performance of the proposed method is now analysed using cubic splines. Fig. 10(a) refers to the displacement based multi-patch formulation. For all the thickness ratios considered, the rate of convergence starts from 2 and tends asymptotically to a super-convergent rate of 5. Fig. 10(b) summarizes the dependency of the  $L^2$  error norm from the thickness ratio. In every case locking is present, although less severely than in the case a quadratic interpolation is used. In this case, the error is smaller than in the previous case and much smaller than the error obtained with a continuous displacement interpolation.

The results obtained with the mixed model are presented in Figs. 11(a) and 11(b). The optimal convergence rate of 4 is reached in this case, and Fig. 11(b) evidences the absence of locking.

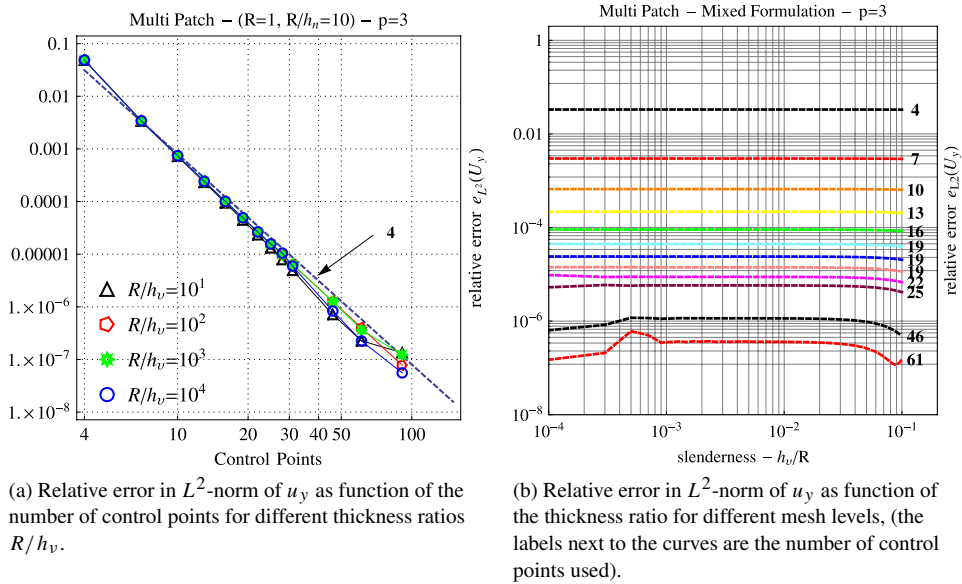


Fig. 11. 2D arch. Mixed formulation with  $G^1$  continuity for third degree polynomial interpolation.

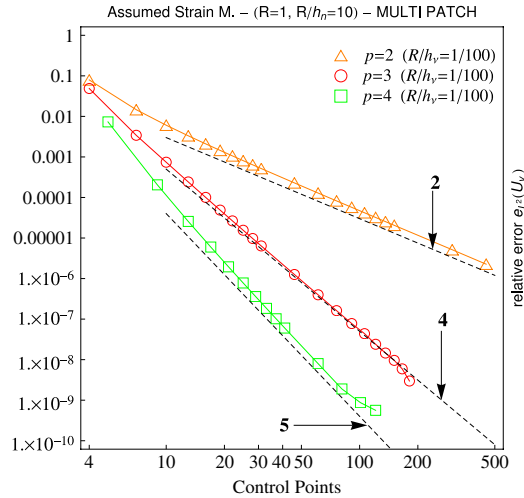


Fig. 12. 2D arch. Mixed multipatch formulation with  $G^1$  continuity. Comparison between interpolations with different polynomial degrees.

The rates of convergence of the mixed multi patch  $G^1$  continuous model for different polynomial degrees are compared in Fig. 12. Optimal rate of convergence is reached, except than for the case  $p = 2$ , as also observed in [48].

### 5.2. Flexural locking: 3D circular arch with a point force at the free end

This example concerns a 3D cantilever circular arch loaded at the tip by a vertical force  $\mathbf{F} = \{0, 0, -1\}$ , (kN). The radius of the centroid curve is  $R = 1$  (m) the section is rectangular with  $h_n = 0.1$  and  $h_v$  is variable,  $\hat{\mathbf{n}}(S) = \mathbf{e}_z$ ,  $\hat{\mathbf{v}} = \hat{\mathbf{t}} \times \mathbf{e}_z$  and  $E = 2.0 \times 10^8$  (kN/m<sup>2</sup>),  $\nu = 0.25$ ; for the geometry see Fig. 13.

This is a typical example in which the flexural locking affects the solution in a displacement based approach. In addition spurious modes are observed that affect the bending moments. Analogously to the analyses carried out in the previous example, the  $L^2$  error norm for the vertical displacement  $u_z(S)$  (the most affected by torsional interaction) is examined.

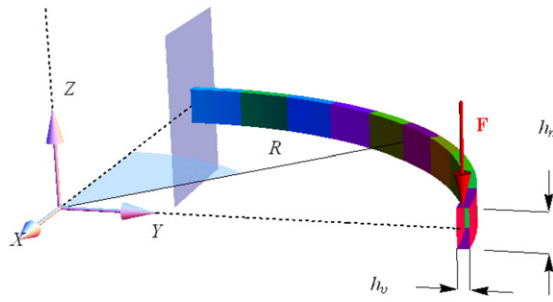


Fig. 13. Geometries of the 3D cantilever arch with a point force at the free end.

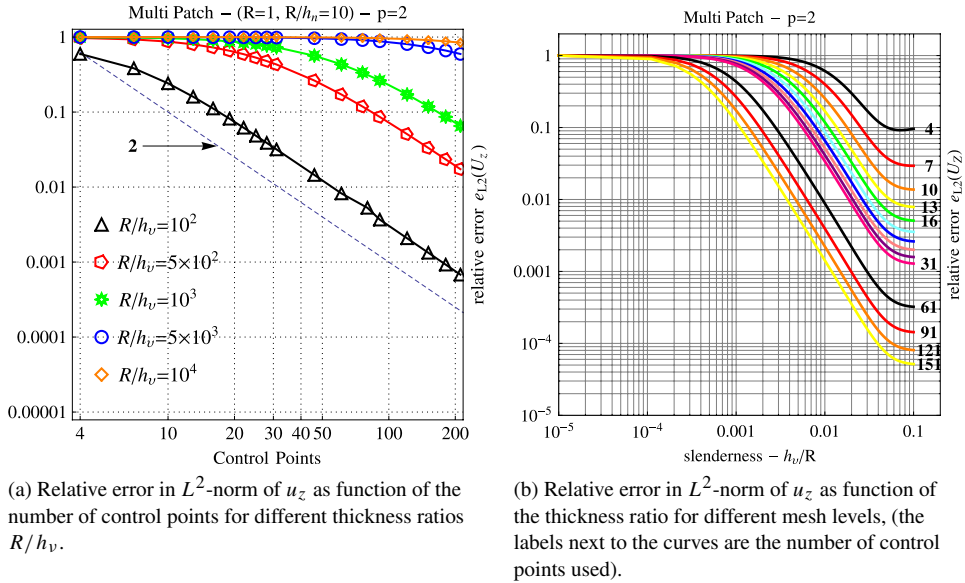


Fig. 14. 3D arch. Displacement based formulation with  $G^1$  continuity for second degree polynomial interpolation.

Figs. 14(a), 14(b) refer to a displacement based solution obtained with a quadratic interpolation. The first shows that a rate of convergence of only 2 is reached. From the second appears that the displacement formulation is unable to correctly reproduce torsional deformations.

The mixed formulation leads to the results presented in Figs. 15(a), 15(b). Again, a suboptimal rate of convergence 2 is obtained, but the error is almost independent from the thickness ratio. The plot of the error versus the thickness ratio shows that a little dependency of the accuracy of the solution on the thickness ratio is still present, so that the solution is not completely free of flexural locking, but the convergence behaviour is guaranteed for a large span of thickness values. The error obtained with the mixed formulation is by a large amount smaller than the error obtained with the displacement formulation.

Similar results are obtained for a cubic interpolation. In this case we present the results obtained for the torsional rotation  $\phi(S)$ . The case of the displacement based multi patch model is summarized in Figs. 16(a), 16(b). The rate of convergence of the solution seems not to match the optimal value  $p + 1$ , at least not for all the thickness ratios investigated. Correspondingly, the accuracy of the solution depends on the thickness ratio (Fig. 16(b)), even though the error is smaller than the one found for the quadratic interpolation.

Examining the results obtained with the mixed formulation, Figs. 17(a), 17(b), it can be observed that the optimal rate of convergence is reached, independently from the thickness ratio, and that the accuracy is almost independent from the thickness ratio, even less than what was found with the second degree interpolation.

Finally the convergence of the  $L^2$  error norm for the vertical displacement  $u_z$  and the rotation  $\phi$  for several polynomial degrees and for the fixed thickness ratio  $R/h_v = 10$  is compared in Figs. 18(a) and 18(b). While the

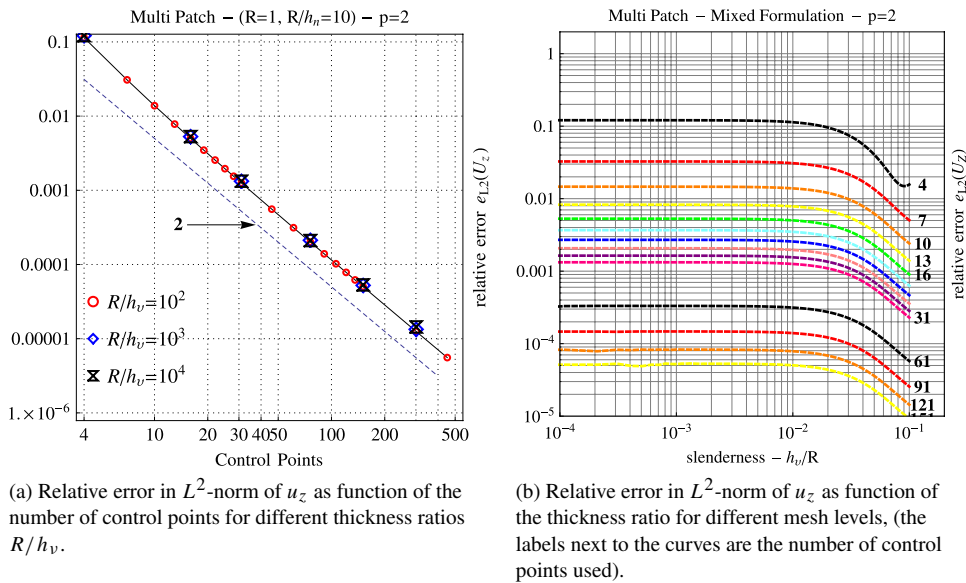


Fig. 15. 3D arch. Mixed formulation with  $G^1$  continuity for second degree polynomial interpolation.

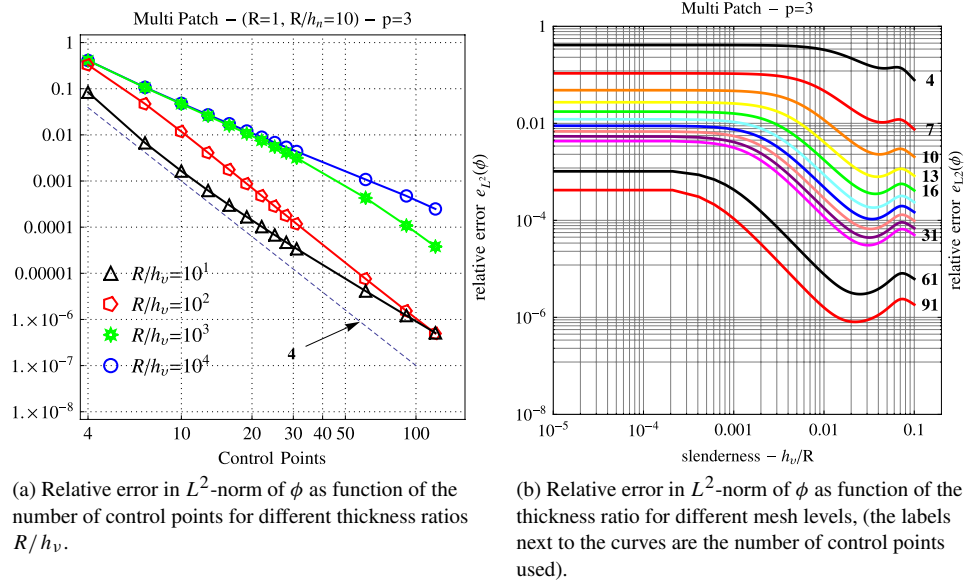


Fig. 16. 3D arch. Displacement based formulation with  $G^1$  continuity for third degree polynomial interpolation.

rate of convergence with the quadratic interpolation is sub-optimal, higher order interpolations reach the optimal rate of convergence. In the case of the torsional rotation, a higher polynomial degree is needed in order to reach the optimal rate of convergence.

Examining the internal forces, the multi-patch displacement based formulation presents strong oscillations in the solution. For instance, the bending moment  $M_v$  is plotted in Figs. 19(a) and 19(b) for thickness ratios 100 and 1000 respectively. In the same figures is plotted the bending moment evaluated with the mixed formulation, that superposes almost exactly to the correct result.

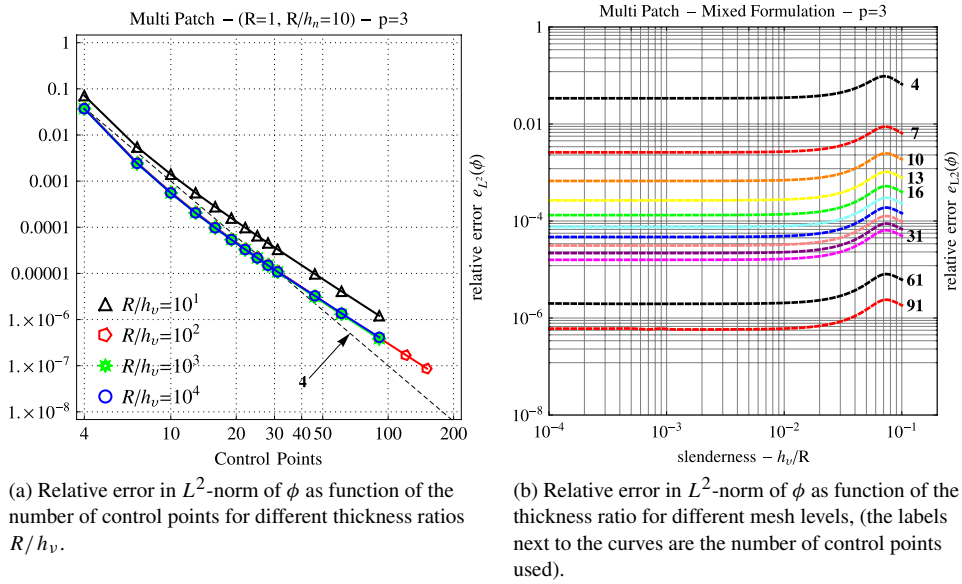


Fig. 17. 3D arch. Mixed formulation with  $G^1$  continuity for third degree polynomial interpolation.

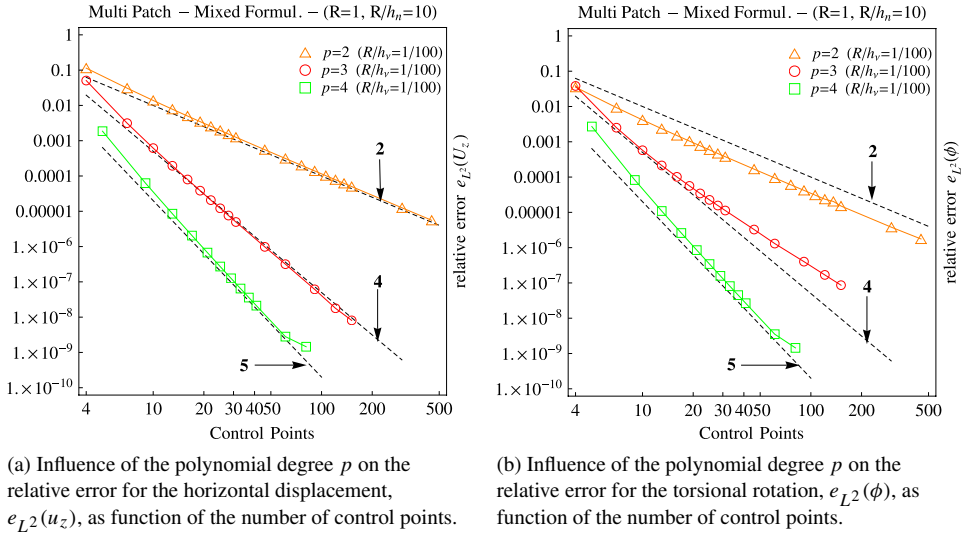


Fig. 18. 3D arch. Mixed formulation with  $G^1$  continuity. Comparison of rate of convergence for different polynomial degrees.

### 5.3. 2D arch with discontinuities in the sectional geometry and in the internal forces

The circular arch of radius  $R = 1$  (m) represented in Fig. 20 is examined. As before,  $\hat{\mathbf{n}} = \hat{\mathbf{e}}_z$ . The width of the arch is  $h_n = 0.1$  (m) while a jump in the thickness  $h_v$  is present, such that  $h_2 = \alpha h_1$ , with  $\alpha$  ranging in the interval  $(1, 10)$ . The arch is loaded at the half arc-length with a point force  $\mathbf{F} = \{0, -1, 0\}$  (kN),  $R = 1$  (m),  $E = 2.0 \times 10^8$  (kN/m<sup>2</sup>).

For a displacement based model the solution is affected by membrane locking. First the case of uniform thickness is considered,  $\alpha = 1$ , ( $h_1 = h_2 = h_v$ ), so that, due to the point force applied, there is a discontinuity on the internal axial and shear forces. A cubic interpolation  $p = 3$  is adopted. Fig. 21(a) shows the rate of convergence and the accuracy of the relative error in  $L^2$ -norm for the vertical displacement component  $u_y$  for several thickness ratios  $R/h_v$ . The accuracy and the rate of convergence depend on the thickness ratio considered, in particular only for the lowest thickness ratio the rate of convergence reaches the theoretical value  $p + 1$ , while increasing the slenderness parameter the rate of convergence of the relative error decreases to the value 2. The results obtained with the B-

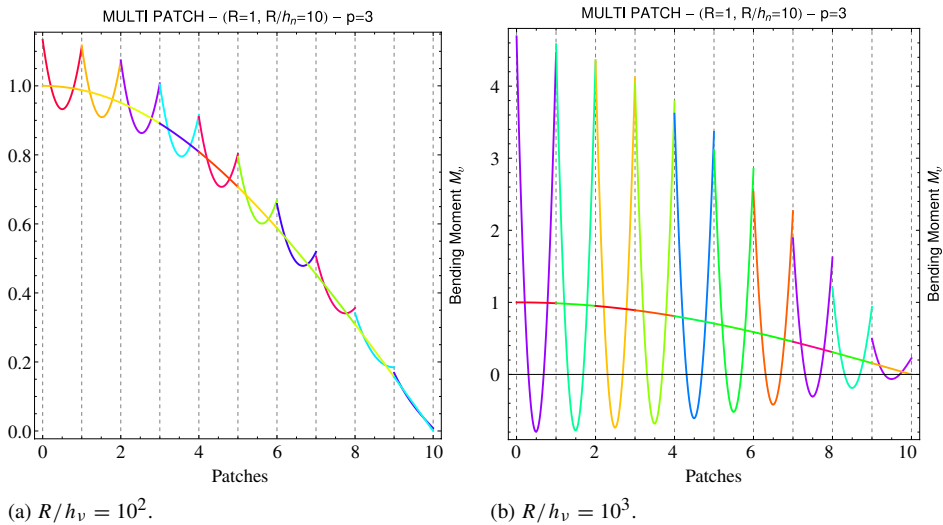


Fig. 19. 3D arch. Bending moment  $M_v$  for multi-patch  $G^1$  continuous displacement formulation and multi-patch  $G^1$  continuous mixed formulation with a third degree polynomial interpolation.

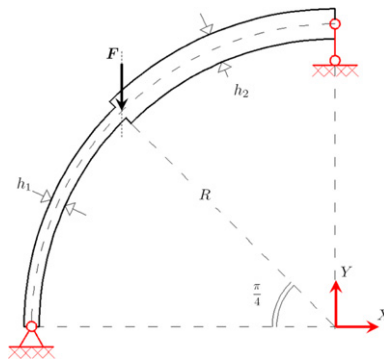


Fig. 20. Geometry for the 2D arch with mid-point force and a jump in the thickness.

bar formulation are presented in Fig. 21(b). The rate of convergence of the relative error in  $L^2$ -norm for the  $u_y$  displacement component is optimal and the accuracy is independent from the thickness ratio.

The deformation of the arch presented in Fig. 22 shows that the  $G^1$ -continuity is implicitly ensured (i.e. the alignments of the three control points at the joints between subsequent patches are respected).

The  $G^1$  continuous formulation allows discontinuities on the strains and internal forces, as shown in Fig. 23 that presents the axial force along the arch. However huge oscillations can be observed in the displacement formulation (Fig. 23(a)). The solution obtained with the mixed formulation is plotted in Fig. 23(b), and reproduces the exact solution. Increasing the thickness ratio  $R/h_v$  the oscillations in the axial force strongly increase for the displacement based formulation. This phenomenon is highlighted in Figs. 24(a) and 24(b) in which the relative errors in  $L^2$ -norm for the axial force and bending moment are plotted versus the slenderness parameter for the displacement based and the mixed formulation ( $\alpha = 1$ ). The smaller the thickness ratio the greater is the error for the displacement based formulation while with the mixed formulation the accuracy is independent on the slenderness parameter for the considered mesh (20-patches).

Figs. 25 and 26 summarize the results for the case in which the geometry of the arch is discontinuous,  $h_2 = \alpha h_1$ . The axial force distribution is analysed. As  $\alpha$  increases the oscillations in the second part of the arch disappear while they remain unchanged in the first part of the arch for the displacement based formulation (see Fig. 25 respectively for  $\alpha = 3, 5, 7, 10$ ). The solution of the mixed method reproduces in any case the exact result.

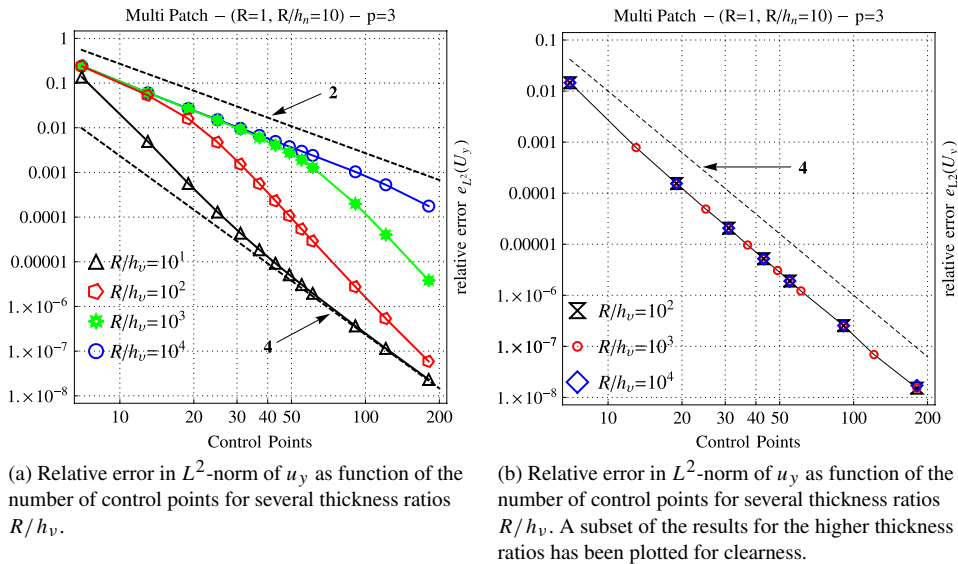


Fig. 21. 2D arch with discontinuity on the internal forces  $\alpha = 1$ . Comparison of the displacement and the mixed formulations for a third degree polynomial interpolation.

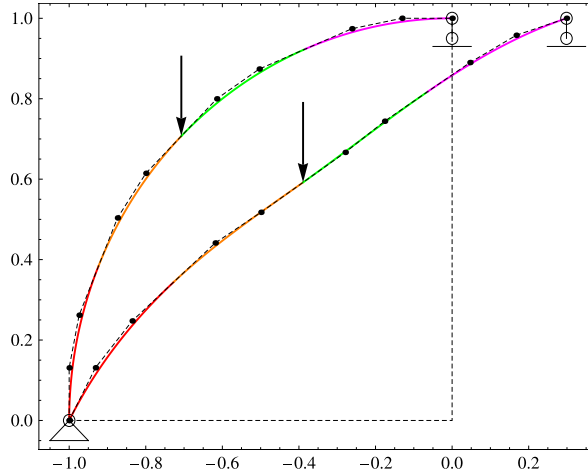
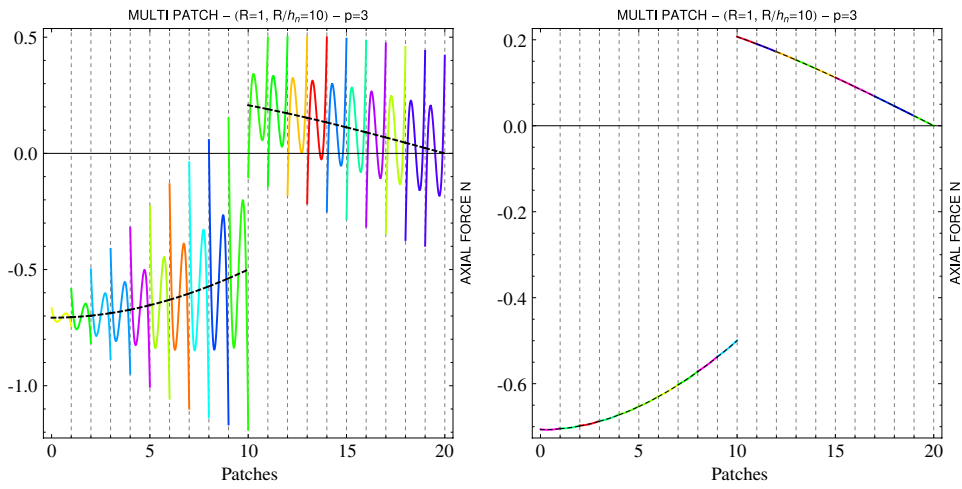


Fig. 22. Initial and deformed geometry ( $\alpha = 1, R/h_v = 10^3$ ).

Figs. 26(a) and 26(b) show the relative errors in the axial force and bending moment for  $R/h_1 = 10^2$  and several values of  $\alpha$  for both the displacement and the mixed formulations. The error in  $L^2$ -norm for the displacement based formulation decreases with increasing values of  $\alpha$  either for the axial force and for the bending moment. In the case of the mixed formulation these errors are independent on the value of  $\alpha$ . Furthermore, the error on the axial force is significantly smaller than the error obtained with the displacement formulation.

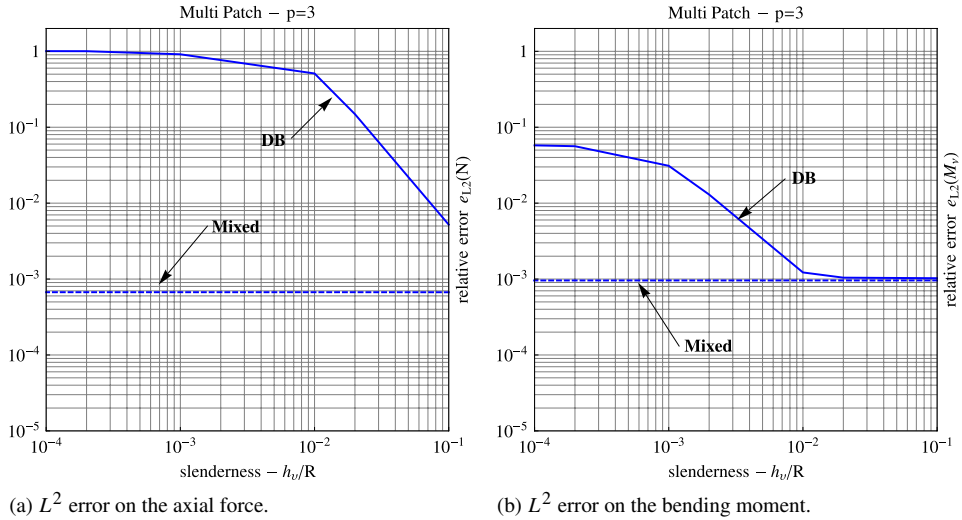
#### 5.4. 3D element with a kink

The previous example presented a plane structure with internal discontinuities. The final example concerns a space structure with a kink and a concentrated force that introduce discontinuities on the bending and torsional moments. The structure represented in Fig. 27(a) is examined, with  $R = 1$  (m),  $\hat{\mathbf{n}} = \hat{\mathbf{e}}_z$ ,  $h_n = 0.1$  (m),  $E = 2 * 10^8$  (kN/m<sup>2</sup>),  $\nu = 0.25$ ,  $\mathbf{F} = (0, 0, -1)$  (kN). The structure is built in at the extremities. The deformed configuration together with the position of the control points is presented in Fig. 27(b). Third degree polynomials were used.



(a) Axial force distribution for the displacement based formulation. The dashed line is the exact solution. (b) Axial force distribution for the mixed formulation.

Fig. 23. 2D arch with a discontinuity on the internal forces ( $\alpha = 1$  and  $h_v = 10^{-2}$  (m)). Diagram of the axial force.



(a)  $L^2$  error on the axial force. (b)  $L^2$  error on the bending moment.

Fig. 24. 2D arch with a discontinuity on the internal forces ( $\alpha = 1$ ).

The bending and torsional moments are plotted in Fig. 28 for  $R/h_v = 10^3$ . Figs. 28(a) and 28(b) refer to  $G^1$  continuous displacement formulation, Figs. 28(c) and 28(d) refer to  $G^1$  continuous mixed formulation. Large oscillations occur in the curved element, especially in the bending moment, and discontinuities in the torsional moment, due to the coupling with the bending displacements. The oscillations and the discontinuities completely disappear in the B-bar formulation.

## 6. Conclusions

A B-bar type formulation for an isogeometric model of space Kirchhoff rods has been presented. A  $G^1$  continuous multi-patch approach has been employed, according to what was proposed in [26]. The approach is very appealing for engineering applications, and, in addition, it allows to effectively use lower order degree interpolations. The mixed formulation is obtained interpolating the internal forces with polynomials of lower degree with respect to

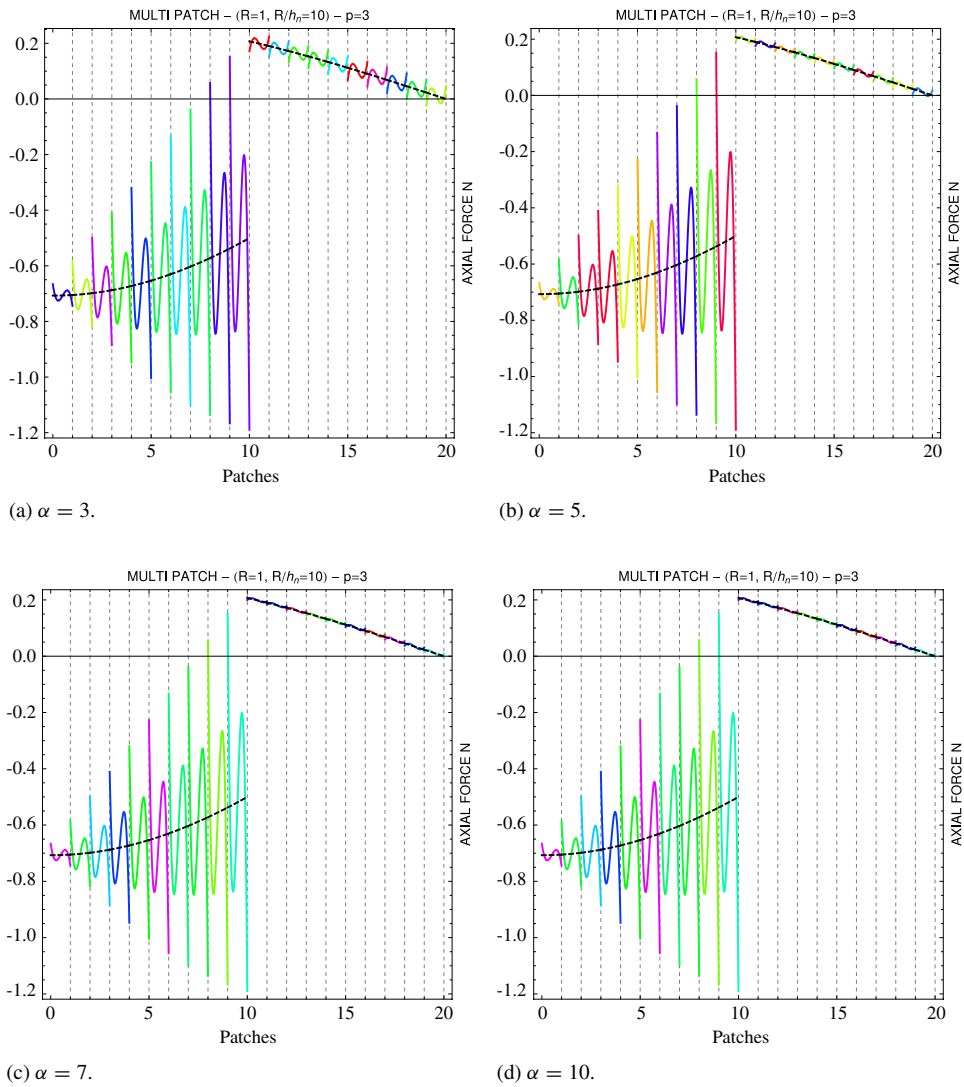
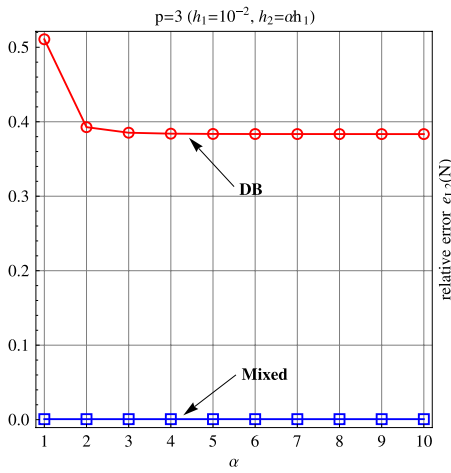


Fig. 25. 2D arch with discontinuity on the geometry,  $h_2 = \alpha h_1$  with  $\alpha = 3, 5, 7, 10$   $h_1 = 10^{-2}$  m. Diagrams of the axial force, displacement and mixed (dashed line) formulations.

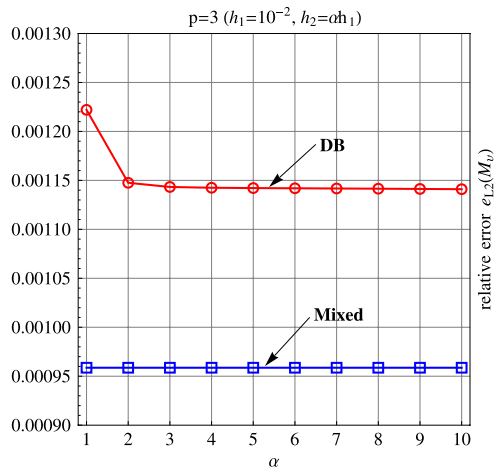
the displacement, leading to a B-bar formulation. The displacement based formulation presents severe locking in all of the examples presented, especially if a single patch interpolation with high continuity is used. Locking is reduced, but is still present, when a multi-patch displacement formulation with  $G^1$  continuity is employed. Using the mixed formulation, on the contrary, locking could be suppressed in the solution, at least for plane problems. In space rods with torsional–flexural interaction, the error was in general found to be independent from the thickness ratio, except for the torsional rotation which showed some residual dependency. In any case the error resulted significantly smaller than the one found for the pure displacement formulation.

As far as the rate of convergence is concerned, it was found that the mixed formulation always reaches the optimal rate of convergence for the  $L^2$  error on the displacements, except for the case in which a quadratic polynomial interpolation was used. The pure displacement solution, instead, generally shows a super convergent rate, but loses accuracy if the slenderness increases.

The mixed approach has proved effective also in reducing the oscillations on the internal forces that are obtained with the displacement formulation for the greatest values of the slenderness and for elements with sharp discontinuities on the geometry or on the internal forces distribution.



(a) Relative errors in  $L^2$ -norm for the axial force for several values of  $\alpha$ .



(b) Relative errors in  $L^2$ -norm for the bending moment for several values of  $\alpha$ .

Fig. 26. 2D arch with discontinuity on the geometry. Axial force and bending moment for  $R/h_1 = 100$ , as function of  $\alpha = h_2/h_1$ .

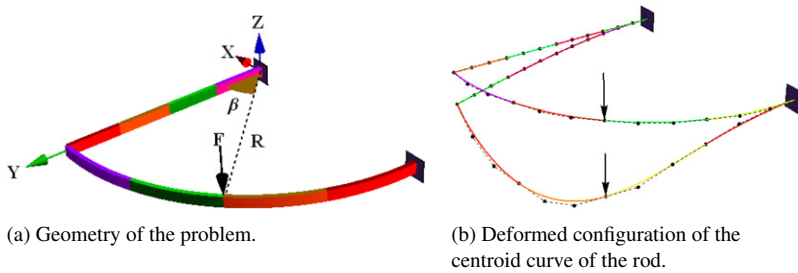


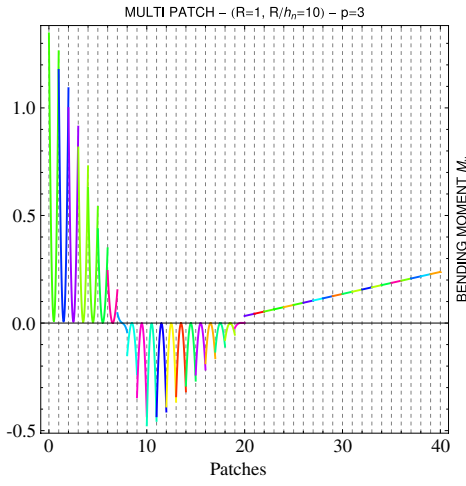
Fig. 27. 3D kinked arch: Geometry and deformed configuration.

## Appendix

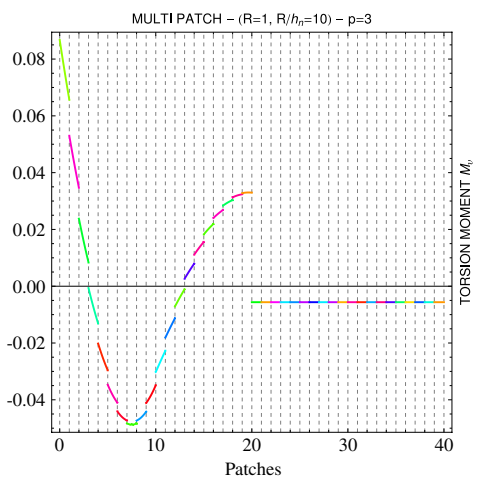
In this appendix we report the explicit form of the deformation matrices introduced in Eq. (23). In the following we denote by  $(t_x, t_y, t_z)$  the component of the tangent vector  $\mathbf{t}$  to the rod axis on a Euclidean frame  $(\mathbf{E}_x, \mathbf{E}_y, \mathbf{E}_z)$ , and indicate by  $\mathbf{b} = \hat{\mathbf{t}} \times \frac{d\hat{\mathbf{t}}}{dS}$  the curvature of the rod axis. Accounting for the results (4) and the interpolation (11) one has:

$$\mathbf{B}_\varepsilon = C_\varepsilon \mathbb{M} \quad C_\varepsilon = \begin{pmatrix} t_x \frac{d}{dS} & 0 & 0 & 0 \\ 0 & t_y \frac{d}{dS} & 0 & 0 \\ 0 & 0 & t_z \frac{d}{dS} & 0 \\ 0 & 0 & 0 & 0 \end{pmatrix} \quad (\text{A.1})$$

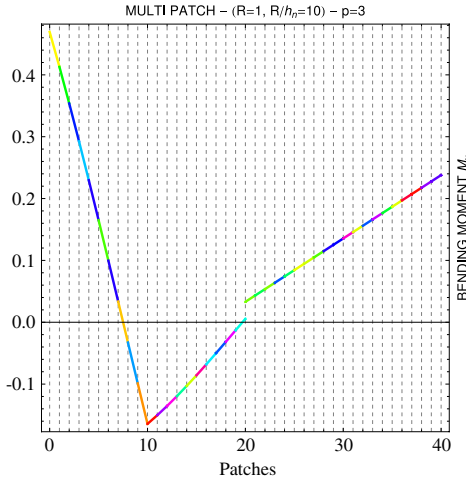
$$\mathbf{B}_{\chi_t} = C_{\chi_t} \mathbb{M} \quad C_{\chi_t} = \begin{pmatrix} \frac{1}{\|\mathbf{t}\|^2} \mathbf{b} \cdot \mathbf{E}_x \frac{d}{dS} & 0 & 0 & 0 \\ 0 & \frac{1}{\|\mathbf{t}\|^2} \mathbf{b} \cdot \mathbf{E}_y \frac{d}{dS} & 0 & 0 \\ 0 & 0 & \frac{1}{\|\mathbf{t}\|^2} \mathbf{b} \cdot \mathbf{E}_z \frac{d}{dS} & 0 \\ 0 & 0 & 0 & \frac{d}{dS} \end{pmatrix} \quad (\text{A.2})$$



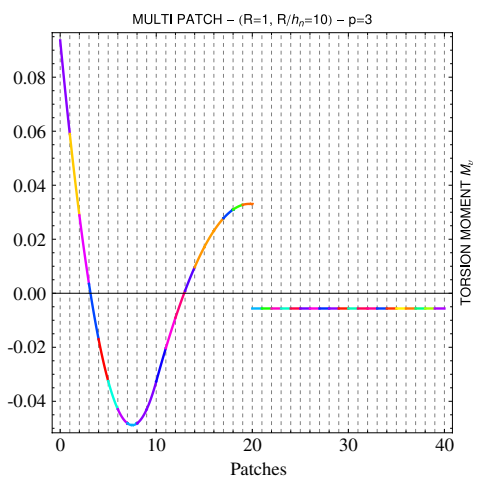
(a) Bending moment distribution for the displacement based formulation.



(b) Torsional moment distribution for the displacement based formulation.



(c) Bending moment distribution for the mixed formulation.



(d) Torsional moment distribution for the mixed formulation.

Fig. 28. 3D kinked arch: Bending and torsional moments for the displacement based and mixed formulation respectively for the thickness  $h_v = 10^{-3}$ .

$$\mathbf{B}_{\chi_n} = \mathcal{C}_{\chi_n} \mathbb{M} \quad \mathcal{C}_{\chi_n} = \begin{pmatrix} -\hat{\mathbf{v}} \cdot \mathbf{E}_x \frac{d^2}{dS^2} & 0 & 0 & 0 \\ 0 & -\hat{\mathbf{v}} \cdot \mathbf{E}_y \frac{d^2}{dS^2} & 0 & 0 \\ 0 & 0 & -\hat{\mathbf{v}} \cdot \mathbf{E}_z \frac{d^2}{dS^2} & 0 \\ 0 & 0 & 0 & \mathbf{b} \cdot \hat{\mathbf{v}} \end{pmatrix} \quad (\text{A.3})$$

$$\mathbf{B}_{\chi_v} = \mathcal{C}_{\chi_v} \mathbb{M} \quad \mathcal{C}_{\chi_v} = \begin{pmatrix} \hat{\mathbf{n}} \cdot \mathbf{E}_x \frac{d^2}{dS^2} & 0 & 0 & 0 \\ 0 & \hat{\mathbf{n}} \cdot \mathbf{E}_y \frac{d^2}{dS^2} & 0 & 0 \\ 0 & 0 & \hat{\mathbf{n}} \cdot \mathbf{E}_z \frac{d^2}{dS^2} & 0 \\ 0 & 0 & 0 & -\mathbf{b} \cdot \hat{\mathbf{n}} \end{pmatrix}. \quad (\text{A.4})$$

## References

- [1] L. Greco, M. Cuomo, B-Spline interpolation for Kirchhoff–Love space rod, *Comput. Methods Appl. Mech. Engrg.* 256 (2013) 251–269.
- [2] L. Greco, M. Cuomo, Consistent tangent operator for an exact Kirchhoff rod model, *Contin. Mech. Thermodyn.* 27 (4–5) (2015) 861–877.
- [3] A. Goriely, M. Nizette, M. Tabor, On the dynamic of elastic strips, *J. Nonlinear Sci.* 11 (1) (2001) 3–45.
- [4] S.B. Raknes, X. Deng, Y. Bazilevs, D.J. Benson, K. Mathisen, T. Kvamsdal, Isogeometric rotation-free bending-stabilized cables: Statics, dynamics, bending strip and coupling with shell, *Comput. Methods Appl. Mech. Engrg.* 263 (2013) 127–143.
- [5] G. Piccardo, L.C. Pagnini, F. Tubino, Some research perspectives in galloping phenomena: critical conditions and post-critical behavior, *Contin. Mech. Thermodyn.* 27 (1–2) (2015) 261–285.
- [6] G. Piccardo, F. Tubino, A. Luongo, A shear-shear torsional beam model for nonlinear aeroelastic analysis of tower buildings, *Z. Angew. Math. Phys.* 66 (4) (2015) 1895–1913.
- [7] D.G. Ashwell, R.H. Gallagher, Limitations of certain curved finite elements when applied to arches, *Int. J. Mech. Sel.* 13 (1971) 133–139.
- [8] D.J. Dawe, Numerical studies using circular arch finite elements, *Comput. Struct.* 4 (1974) 729–740.
- [9] J.E.F. Guimaraes, G.R. Heppler, Trigonometric basis functions for  $C^1$  curved beam finite elements, *Comput. Struct.* 45 (1992) 405–413.
- [10] M. Ishaquddin, P. Raveendranath, J. Reddy, Flexure and torsion locking phenomena in out-of-plane deformation of Timoshenko curved beam element, *Finite Elem. Anal. Des.* 51 (2012) 22–30.
- [11] J. Langer, D. Singer, Lagrangian aspects of the Kirchhoff elastic rod, *SIAM Rev.* 38 (1995) 605–618.
- [12] J.J. Alibert, P. Seppecher, F. dell’Isola, Truss modular beams with deformation energy depending on higher displacement gradients, *Math. Mech. Solids* 8 (1) (2003) 51–73.
- [13] N. Auffray, F. dell’Isola, V. Eremeyev, A. Madeo, G. Rosi, Analytical continuum mechanics á la Hamilton-Piola: least action principle for second gradient continua and capillary fluids, *Math. Mech. Solids* 20 (4) (2015) 375–417.
- [14] F. dell’Isola, H. Gouin, P. Seppecher, Radius and surface tension of microscopic bubbles by second gradient theory, *C. R. Acad. Sci. Série Iib* 320 (1995) 211–216.
- [15] F. dell’Isola, A. Madeo, L. Placidi, Linear plane wave propagation and normal transmission and reflection at discontinuity surfaces in second gradient 3D Continua, *Z. Angew. Math. Mech.* 92 (1) (2012) 52–71.
- [16] L. Placidi, G. Rosi, G. Giorgio, A. Madeo, Reflection and transmission of plane waves at surfaces carrying material properties and embedded in second-gradient materials, *Math. Mech. Solids* 19 (5) (2014) 555–578.
- [17] G. Rosi, I. Giorgio, V.A. Eremeyev, Propagation of linear compression waves through plane interfacial layers and mass adsorption in second gradient fluids, *ZAMM Z. Angew. Math. Mech.* 93 (12) (2013) 914–927.
- [18] C. Gontier, C. Vollmer, A Large displacement analysis of beam using a CAD geometric definition, *Comput. Struct.* 57 (6) (1995) 981–989.
- [19] J.C. Simo, L. Vu-Quoc, A Three dimensional finite strain rod model. Part II: computational aspect, *Comput. Methods Appl. Mech. Engrg.* 58 (1986) 79–116.
- [20] A.P. Nagy, M.M. Abdalla, Z. Gurdal, Isogeometric sizing and shape optimization of beam structures, *Comput. Methods Appl. Mech. Engrg.* 199 (17–20) (2010) 1216–1230.
- [21] J. Cottrell, T. Hughes, A. Reali, Studies of refinement and continuity in isogeometric structural analysis, *Comput. Methods Appl. Mech. Engrg.* 196 (2007) 4160–4183.
- [22] J. Lu, X. Zhou, Cylindrical element: Isogeometric model of continuum rod, *Comput. Methods Appl. Mech. Engrg.* 200 (1–4) (2011) 233–241.
- [23] F. Auricchio, L.B. da Veiga, J. Kiendl, C. Lovadina, A. Reali, Locking-free isogeometric collocation methods for spatial Timoshenko rods, *Comput. Methods Appl. Mech. Engrg.* 263 (2013) 113–126.
- [24] A. Cazzani, M. Malagú, E. Turco, Isogeometric analysis of plane-curved beams, *Math. Mech. Solids* (2014), <http://dx.doi.org/10.1177/1081286514531265>.
- [25] A. Cazzani, M. Malagú, E. Turco, F. Stochino, Constitutive models for strongly curved beams in the frame of isogeometric analysis, *Math. Mech. Solids* (2015), <http://dx.doi.org/10.1177/108128651557704>.
- [26] L. Greco, M. Cuomo, An implicit  $G^1$  multi patch B-spline interpolation for Kirchhoff–Love space rod, *Comput. Methods Appl. Mech. Engrg.* 269 (2014) 173–197.
- [27] L. Greco, M. Cuomo, Multi-patch isogeometric analysis of space rods, in: 11th International Conference on Computational Structures Technology, in: *Civil Comp Proceeding*, vol. 99, Dubrovnik, 4–7 September, 2012, pp. 5094–5112.
- [28] J. Kiendl, Y. Bazilevs, M.-C. Hsu, R. Wuchner, K.-U. Bletzinger, The bending strip method for isogeometric analysis of Kirchhoff–Love shells structures comprised of multiple patches, *Comput. Methods Appl. Mech. Engrg.* 199 (2010) 2403–2416.
- [29] D. Benson, S. Hartmann, Y. Bazilevs, M.-C. Hsu, T. Hughes, Blended isogeometric shells, *Comput. Methods Appl. Mech. Engrg.* 255 (2013) 133–146.
- [30] R. Echter, M. Bischoff, Numerical efficiency, locking and unlocking of NURBS finite elements, *Comput. Methods Appl. Mech. Engrg.* 199 (2010) 374–382.
- [31] L.B. da Veiga, C. Lovadina, A. Reali, Avoiding shear locking for the Timoshenko beam problem via isogeometric collocation methods, *Comput. Methods Appl. Mech. Engrg.* 241–244 (2012) 38–51.
- [32] R. Bouclier, T. Elguedj, A. Combescure, Locking free isogeometric formulations of curved thick beams, *Comput. Methods Appl. Mech. Engrg.* 245–246 (2012) 144–162.
- [33] F. Armero, J. Valverde, Invariant Hermitian finite elements for thin Kirchhoff rods. I: The linear plane case, *Comput. Methods Appl. Mech. Engrg.* 213–216 (2012) 427–457.
- [34] F. Armero, J. Valverde, Invariant Hermitian finite elements for thin Kirchhoff rods. II: The linear three-dimensional case, *Comput. Methods Appl. Mech. Engrg.* 213–216 (2012) 458–485.

- [35] L. Greco, M. Cuomo, N. Impollonia, An unlocked implicit  $G^1$  continuity multi patch B-Spline interpolation for the analysis of 3D Kirchhoff–Love rod elements, in: M. Papadrakakis, M. Kojic, I.Tuncer (Eds.), SEECMIII, 3rd South-European Conference on Computational Mechanics, 12–14 June, Kos Island, Greece, 2013.
- [36] M. Cuomo, L. Greco, Isogeometric analysis of space rods: Considerations on stress locking, in: European Congress on Computational Methods in Applied Sciences and Engineering, 10–14 September, Vienna, 2012, pp. 5094–5112.
- [37] K.-U. Bletzinger, M. Bischoff, E. Ramm, A unified approach for shear-locking free triangular and rectangular shell finite elements, *Comput. Struct.* 75 (2000) 321–334.
- [38] F. Auricchio, L.B. da Veiga, J. Kiendl, C. Lovadina, A. Reali, Locking-free isogeometric collocation methods for spatial Timoshenko rods, *Comput. Methods Appl. Mech. Engrg.* 263 (2013) 113–126.
- [39] J. Kiendl, F. Auricchio, T. Hughes, A. Reali, Single-variable formulations and isogeometric discretizations for shear deformable beams, *Comput. Methods Appl. Mech. Engrg.* 284 (2015) 988–1004.
- [40] T. Elguedj, Y. Bazilevs, V.M. Calo, T.J.R. Hughes, B-bar and F-bar projection methods for nearly incompressible linear and non linear elasticity and plasticity using higher order NURBS element, *Comput. Methods Appl. Mech.* 197 (2007) 5257–5296.
- [41] P.G. Lee, H.C. Sin, Locking free curved beam element based on curvature, *Int. J. Numer. Methods Engrg.* 37 (1994) 989–1007.
- [42] R. Bouclier, T. Elguedj, A. Combesure, Efficient isogeometric NURBS-based solid-shell elements: Mixed formulation and  $\bar{B}$ -method, *Comput. Methods Appl. Mech. Engrg.* 267 (2013) 86–110.
- [43] A. Luongo, A.D. Egidio, Divergence, Hopf and double-zero bifurcations of a nonlinear planar beam, *Comput. Struct.* 84 (24–25) (2006) 1596–1605.
- [44] F. Maurin, L. Dedé, A. Spadoni, Isogeometric rotation-free analysis of planar extensible-elastica for static and dynamic applications, *Nonlinear Dynam.* 81 (2015) 77–96.
- [45] B.A. Barsky, T.D. DeRose, Geometric continuity of parametric curves: Three equivalent characterizations, *IEEE Comput. Graph. Appl.* 9 (6) (1989) 60–68.
- [46] M.E. Hohmeyer, B.A. Barsky, Rational continuity: Parametric, geometric, and frenet frame continuity of rational curves, *ACM Trans. Graph.* 8 (4) (1989) 335–359.
- [47] S.T. Yeo, B.C. Lee, Equivalence between enhanced assumed strain method and assumed stress hybrid method based on the Hellinger-Reissner Principle, *Int. J. Numer. Methods Engrg.* 39 (1996) 3083–3099.
- [48] L. Noels, R. Radovitzky, A new discontinuous Galerkin method for Kirchhoff–Love shells, *Comput. Methods Appl. Mech. Engrg.* 197 (2008) 2901–2929.